ESTIMATION OF EXPECTED EULER CHARACTERISTIC CURVES OF NONSTATIONARY SMOOTH RANDOM FIELDS

BY FABIAN J. E. TELSCHOW[1,a], DAN CHENG[2,b], PRATYUSH PRANAV[3,c] AND ARMIN SCHWARTZMAN[4,d]

[1]*Department of Mathematics, Humboldt-Universität zu Berlin,* [a]*fabian.telschow@hu-berlin.de*

[2]*School of Mathematical and Statistical Sciences, Arizona State University,* [b]*chengdan@asu.edu*

[3]*Centre de Recherche Astrophysique de Lyon,* [c]*pratyuze@gmail.com*

[4]*Halıcıoğlu Data Science Institute, University of California, San Diego,* [d]*a7schwartzman@ucsd.edu*

The expected Euler characteristic (EEC) of excursion sets of a smooth Gaussian-related random field over a compact manifold approximates the distribution of its supremum for high thresholds. Viewed as a function of the excursion threshold, the EEC of a Gaussian-related field is expressed by the Gaussian kinematic formula (GKF) as a finite sum of known functions multiplied by the Lipschitz–Killing curvatures (LKCs) of the generating Gaussian field. This paper proposes consistent estimators of the LKCs as linear projections of "pinned" Euler characteristic (EC) curves obtained from realizations of zero-mean, unit variance Gaussian processes. As observed, data seldom is Gaussian and the exact mean and variance is unknown, yet the statistic of interest often satisfies a CLT with a Gaussian limit process; we adapt our LKC estimators to this scenario using a Gaussian multiplier bootstrap approach. This yields consistent estimates of the LKCs of the possibly nonstationary Gaussian limiting field that have low variance and are computationally efficient for complex underlying manifolds. For the EEC of the limiting field, a parametric plug-in estimator is presented, which is more efficient than the nonparametric average of EC curves. The proposed methods are evaluated using simulations of 2D fields, and illustrated on cosmological observations and simulations on the 2-sphere and 3D fMRI volumes.

1. Introduction.

1.1. *The expected Euler characteristic curve.* The expected Euler characteristic curve (EEC) is a function of a real valued parameter—the excursion threshold. The EEC summarizes the topology of the excursion sets of a random field above the excursion threshold in terms of its expected Euler characteristic. For large thresholds, the EEC is an excellent approximation of the tail distribution of the supremum of a zero-mean, unit-variance, smooth Gaussian field defined over a compact domain [33]. Therefore, it has been used to set the significance threshold for control of the familywise error rate (FWER), particularly in neuroimaging studies [27, 41, 42]. More recently, it has been shown to give close to nominal coverage for simultaneous confidence bands for functional data with sufficiently regular sample paths, even for small sample sizes [24, 38, 39] and simultaneous spatial inclusion of spatial excursion sets [32]. The EEC has also been utilized to test Gaussianity of a sample of stationary and isotropic processes [7, 14, 37].

The strength of the EEC lays in the fact that it can be written explicitly for Gaussian fields (and Gaussian-related fields) by means of the Gaussian kinematic formula (GKF) [5, 34].

This formula ingeniously connects geometric and probabilistic properties of a smooth zero-mean, unit-variance, Gaussian field f defined over a compact D-dimensional manifold S with or without boundary. It states that the EEC of the excursion set $A_f(u) = \{s \in S : f(s) \geq u\}$ can be written as

$$
(1) \qquad \text{EEC}(u) = \mathbb{E}\big[\chi\big(A_f(u)\big)\big] = \mathcal{L}_0 \Phi^+(u) + \sum_{d=1}^{D} \mathcal{L}_d \rho_d(u),
$$

which remarkably is a finite linear combination of the so-called EC-densities

$$
(2) \qquad \rho_d(u) = (2\pi)^{-(d+1)/2} H_{d-1}(u) e^{-u^2/2}, \quad d \in \{1, \dots, D\},
$$

where H_d is the dth probabilistic Hermite polynomial and $\Phi^+(u) = \mathbb{P}(\mathcal{N}(0,1) \geq u)$. The linear coefficients $\mathcal{L}_0, \dots, \mathcal{L}_D$ are called *Lipschitz–Killing curvatures* (LKCs) of S and are intrinsic volumes of S considered as a Riemannian manifold endowed with a Riemannian metric induced by f; compare [5], Chapter 12. In applications, except for $\mathcal{L}_0 = \chi(S)$, which is simply the EC of S, the LKCs $\mathcal{L}_1, \dots, \mathcal{L}_D$ need to be estimated since they depend on the unknown correlation function of f.

1.2. *Previous work on estimation of LKCs.* Estimation of LKCs was first studied in the neuroimaging community assuming that the random field is stationary isotropic [22, 40, 41]. These estimators use the fact that for isotropic fields the LKCs are simple functions of the covariance matrix of first-order partial derivatives of f [5], Corollary 11.7.3. Thus, sophisticated discrete derivatives based on i.i.d. observations $f_1, \dots, f_N \sim f$ and averaging across S gives accurate estimates of the LKCs. The simplifying stationary isotropic assumption has been recently called into question in neuroimaging studies, claiming that it has led to too many false positive findings and lack of reproducibility [15].

A major complication in removing this strong assumption is that even knowing the functional form of a nonstationary covariance function exactly is generally not helpful. While the LKCs can be written as integrals of covariances of partial derivatives of the field [5], Theorem 12.4.2, these integrals are hard to evaluate analytically or numerically for manifolds S of dimension $D > 1$.

Currently, there are two approaches in the literature that relax this strong assumption on f. In [35], an estimator was introduced based on triangulating S and warping the mesh of vertices using a diffeomorphism $\psi : S \to S$ such that the random field $f \circ \psi$ on the triangulated domain becomes approximately locally isotropic. This combined with smart computation of intrinsic volumes for simplicial complexes yields an LKC estimator, called the *warping estimator* hereafter. It does not require stationarity, and since it can be based on normalized residuals, it can be applied to fields f with unknown mean and variance. Moreover, if the triangulation of S gets infinitely dense and the field f is Gaussian, the warping estimator is unbiased. An apparent downside of the warping estimator is its conceptual complexity and being difficult to implement in software, especially for complex domains such as subsets of spheres.

A more recent still unpublished approach, which inspired our work, is based on regression [4]. Following the form of (1), they proposed to perform a linear regression of the average of empirically observed EC curves of a sample $f_1, \dots, f_N \sim f$ on the EC-densities. Choosing a set $u_1, \dots, u_P \in \mathbb{R}$ of exceedance levels transforms estimation of the LKCs into a general linear model with known covariates $\rho_d(u_p)$. The regression coefficients $\mathcal{L}_1, \dots, \mathcal{L}_D$ are estimated by weighted least squares.

This approach, which they call *LKC regression*, has several problems. First, there are no clear guidelines on how to choose the locations $u_1, \dots, u_P$ on the real line, and the

authors only compare heuristics for their placement. Second, the covariance function of the error vector of the regression needs to be estimated, which is equivalent to estimating $\mathrm{Cov}[\chi(A_{u_p}), \chi(A_{u_{p'}})]$ for $p, p' \in \{1, \ldots, P\}$. Unfortunately, not much is known about this quantity for general Gaussian random fields yet, including under which conditions it is guaranteed to even exist. Third, no theoretical analysis of LKC regression is given providing, for example, unbiasedness or consistency. And fourth, most importantly, it relies heavily on observing zero-mean, unit-variance Gaussian samples. As we show in simulations, the empirical mean of the observed EC curves is not a consistent estimator of the EEC of a mean-zero, unit-variance Gaussian process, if the sample is not itself sampled from such a process because the empirical EEC obtained from such a sample, which is used as the input data in the regression, is not centered at an EEC of a Gaussian field. Hence for non-Gaussian observations or if it is unknown whether the generating Gaussian random field is zero-mean and unit-variance, LKC regression is always biased. This renders LKC regression, as given, inapplicable in most practical situations.

1.3. *Our proposed Hermite projection estimator.* Inspired by the regression approach, our proposed estimator solves all its problems. The key observation is that the EC densities (2), appropriately scaled, form an orthonormal system for a weighted L^2 space. Thus, the dth LKC coefficient can be obtained by an appropriate orthogonal projection of the EEC onto the dth EC density. We call this the *Hermite projection estimator* (HPE) of the LKCs. In Theorem 1, we show that the HPE for zero-mean, unit-variance Gaussian fields can be efficiently computed without numerically solving the indefinite integral that defines the projection. Under slightly stronger conditions than those required by the GKF, we prove in Theorem 2 that the estimator is unbiased, and under an additional mild assumption, has finite variance. These results allow us, by using the strong law of large numbers and the standard multivariate CLT, to draw power for estimating the LKCs from a sample $f_1, \ldots, f_N$, proving consistency and under further conditions that the HPE satisfies a CLT. A byproduct of the proof of Theorem 2 is the property that $\mathrm{Cov}[\chi(u), \chi(u')]$ decays faster than any polynomial in u, u'; see Corollary 1. This result has value on its own, since it gives a partial answer to the conjectured property that the variance $\mathrm{Var}[\chi(u)]$ decays exponentially in u (Robert Adler, private communication).

The HPE still requires zero-mean, unit-variance Gaussian fields to work properly, as illustrated in our simulations. To solve this problem, we prove in Theorem 3 that, under appropriate conditions on an estimator of derivatives of the correlation function of the random field, the LKCs can be consistently estimated. Implementing this estimator is complicated in practice for complex domains S. We circumvent this problem by an unusual use of the Gaussian multiplier bootstrap, which allows us to estimate the LKCs of a Gaussian limiting field f from non-Gaussian observations $f_1, \ldots, f_N$. The Gaussian multiplier bootstrap simulates sample paths from a Gaussian field, which for a given observed sample, are zero-mean, unit-variance with correlation function being the sample correlation. The obtained fields from the Gaussian multiplier bootstrap can be fed into the HPE to obtain consistent LKC estimates of the Gaussian limiting field f. We call this estimator the *bootstrapped HPE* (bHPE), which removes the dependency on Gaussian observations and has a lower variance than the HPE even for Gaussian observations.

As proposed in [4], the EEC of a Gaussian field can be estimated by plugging an LKC estimate into the right-hand side of (1). For a Gaussian-related field, its EEC can be estimated similarly by using its GKF. If based on a single observed field, we refer to the corresponding EC curve as *smoothed EC curve*. This is illustrated for an isotropic field in Figure 1. Using the HPE/bHPE for the LKCs and averaging the smoothed EC curves for multiple realizations leads to a linear and smooth parametric estimator of the EEC, which we also call HPE/bHPE.
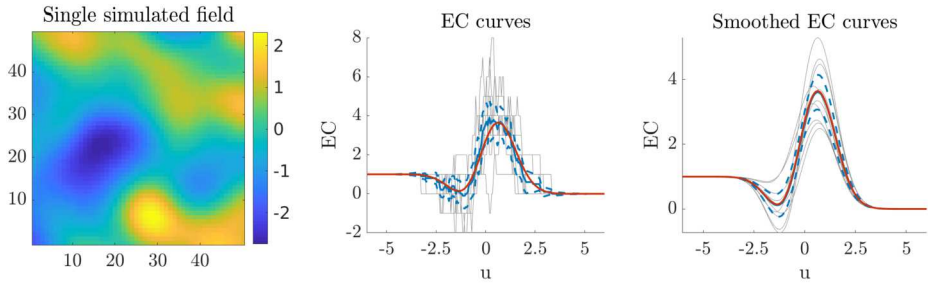
FIG. 1. (left) Realization of the Gaussian random field equation (28) over a 49×49 grid. (middle) EC curves (gray) for $N = 10$ realizations of the field and their average (blue). (right) Corresponding smoothed EC curves (gray) and their pointwise average (blue). Dashed blue lines are pointwise 95% confidence bands for the true EEC (red).

This estimator satisfies a functional central limit theorem (fCLT) (see Proposition 2) from which we can get confidence bands. Alternatively, a nonparametric estimate may be obtained by pointwise averaging the observed EC curves; compare Figure 1 (middle). Simulations show that the HPE has a lower variance. This can be explained by the fact that the HPE is an orthogonal projection of the nonparametric estimator onto the EC densities. Additionally, for applications in FWER inference, Theorem 4 shows that our EEC estimator leads to a consistent estimator of the detection threshold and derives confidence intervals for it.

1.4. *Simulations and data applications.* The simulations in Section 5 study the finite sample performance of the HPE and bHPE for Gaussian, non-Gaussian and nonstationary fields on a 2D rectangular domain. Performances are compared to a method (IsotE) [22] tailored to stationary isotropic fields and the warping estimator (WarpE) [35], which applies to nonisotropic fields. In all cases, the bHPE gives comparable or better results than its competitors.

In Section 6, we estimate EECs of the cosmic microwave background (CMB) radiation field on a complex, nontrivial subset of the 2-sphere using cosmological simulations [2] in order to compare the physical model with actual observed CMB data from the Planck satellite [6]. A second data application for FWER inference on voxelwise activation in a single-subject fMRI study [26] is available in the Supplementary Material [36]. Matlab code reproducing the simulation results and data analysis is available under https://github.com/ftelschow/HPE. The most recent implementation of the HPE and bHPE and other LKC estimators can be found in the RFTtoolbox https://github.com/sjdavenport/RFTtoolbox.

2. Estimation of the LKCs for Gaussian fields.

2.1. *Setting and assumptions.* Let S be a D-dimensional, compact, orientable $\mathcal{C}^2$-manifold with or without boundary. If S does not have a boundary, let $\tilde{S} = S$; otherwise let $\tilde{S}$ be a D-dimensional, $\mathcal{C}^3$-manifold without boundary such that $S \subset \tilde{S}$ is a compact, $\mathcal{C}^2$-submanifold and its boundary ∂S is a $(D-1)$-dimensional $\mathcal{C}^2$-submanifold. Recall that (U, ϕ) is a $\mathcal{C}^2$-chart around $s \in \tilde{S}$ if $U \subset \tilde{S}$ is open and contains s, and $\phi \in \mathcal{C}^2(U, V)$ is a diffeomorphism onto an open set $V \subset \mathbb{R}^D$. By the compactness of S, there is a finite atlas $(U_\alpha, \phi_\alpha)_{\alpha \in \{1, \ldots, P\}}$ of S, $P \in \mathbb{N}$, derived from charts $(\tilde{U}_\alpha, \tilde{\phi}_\alpha)_{\alpha \in \{1, \ldots, P\}}$ of $\tilde{S}$ such that $U_\alpha = \tilde{U}_\alpha \cap S$ and $\phi_\alpha : U_\alpha \to V_\alpha = \tilde{\phi}_\alpha(\tilde{U}_\alpha \cap S)$ is the restriction of $\tilde{\phi}_\alpha$ to U_α. Denote with $f_\alpha = f \circ \phi_\alpha^{-1}$ the coordinate representation of f in the chart U_α and denote with ∇f_α the gradient and with $\nabla^2 f_\alpha$ the Hessian of f_α. Furthermore, define the number of critical points

N_f of f and $N_{f,v}$ the number of critical points of f with critical values larger than $v \in \mathbb{R}_{>0}$ by

$$N_f = \#\{s \in S : \nabla f_\alpha(\phi_\alpha(s)) = 0 \text{ for an } \alpha \in \{1, \ldots, P\}\},$$

$$N_{f,v} = \#\{s \in S : \nabla f_\alpha(\phi_\alpha(s)) = 0 \text{ for an } \alpha \in \{1, \ldots, P\} \text{ and } |f(s)| > v\}$$

We introduce the following abbreviations $u_0 = \min_{s \in S} f(s)$ for the global minimum and $u_M = \max_{s \in S} f(s)$ for the global maximum of f. Finally, let $\mathbf{vech}(A)$ denotes the *half-vectorization* of a symmetric matrix $A \in \mathbb{R}^{D \times D}$, that is,

$$\mathbf{vech}(A) = (A_{11}, \ldots, A_{D1}, A_{22}, \ldots, A_{D2}, \ldots, A_{D-1D-1}, A_{DD-1}, A_{DD}).$$

The assumptions required to prove our main results of this section are:

(G1) f is a zero-mean, unit-variance Gaussian field on $\tilde{S}$ with a.s. $\mathcal{C}^2$-sample paths.
(G2) For all $\alpha \in \{1, \ldots, P\}$, the covariance matrices of the Gaussian vector

$$\big(f_\alpha(x), \nabla f_\alpha(x), \mathbf{vech}(\nabla^2 f_\alpha(x))\big)$$

is nondegenerate for all $x \in V_\alpha$.
(G3) For all $\alpha \in \{1, \ldots, P\}$, there exist constants $K > 0$ and $\gamma > 0$ such that

$$\mathbb{E}\left[\left(\frac{\partial^2 f_\alpha}{\partial x_d \partial x_{d'}}(x) - \frac{\partial^2 f_\alpha}{\partial x_d \partial x_{d'}}(y)\right)^2\right] \leq K \|x - y\|^{2\gamma}$$

for all $x, y \in V_\alpha$ and all $d, d' \in \{1, \ldots, D\}$.
(G4) Assume there exists some $v > 0$ (possibly very large) such that

    (a) $\mathbb{E}[N_{f,v} \mathbb{1}_{\{u_0 < u \leq u_M\}}] = \mathcal{O}(u^{-D-2})$.

    (b) $\mathbb{E}[N_f^2] < \infty$, $\mathbb{E}[N_{f,v} N_f \mathbb{1}_{\{u_0 < u \leq u_M\}}] = \mathcal{O}((u)^{-D-2})$,

        $\mathbb{E}[N_{f,v}^2 \mathbb{1}_{\{u_0 < u \leq u_M\}} \mathbb{1}_{\{u_0 < u' \leq u_M\}}] = \mathcal{O}((uu')^{-D-2})$

as $|u|, |u'| \to \infty$.

REMARK 1. The conditions **(G1)**–**(G3)** are required for the GKF [5], Theorem 12.4.1, Theorem 12.4.2, and only conditions **(G3)** is only slightly stronger for simplicity than what is needed; compare [5], Corollary 11.3.2. In particular, they imply that the paths of f are almost surely Morse functions [5], Chapter 11.3.

REMARK 2. Condition **(G4a)** is required to show that the HPE is unbiased and Condition **(G4b)** implies that the covariance matrix of the HPE exists. In particular, the bootstrapped HPE only requires **(G4a)** for the Gaussian multiplier field to obtain a consistent estimator of the LKCs; compare Section 3. Finite variance and a CLT for the bHPE depend on properties of the estimate of the Riemannian metric induced by f on S and can be established using the delta method; see Section 3.1.

REMARK 3. In Appendix A.4, we show using Borel TIS inequality [5], Theorem 2.1.1., and Hölder's inequality that **(G4a)** and **(G4b)** are satisfied if high enough moments of the number of critical points of f exists.

In particular, **(G4a)** follows from $\mathbb{E}[N_{f,v}^{1+\epsilon}] < \infty$ for some $\epsilon > 0$. The latter is a mild assumption because Lemma 3 from [28] can be used to show $\mathbb{E}[N_{f,v}^2] < \infty$ under conditions very similar to **(G1)**–**(G3)**. Moreover, replacing **(G2)** by a slightly stronger assumption [12] established that $\mathbb{E}[N_f^2] < \infty$ and, therefore, **(G4a)** is satisfied for many processes satisfying the GKF, that is, **(G1)**–**(G3)**.

Recently, it even has been proven that $\mathbb{E}[N_f^p] < \infty$, if the sample paths of f are almost surely $\mathcal{C}^{p+1}$ and a nondegeneracy condition similar to **(G2)** holds true, which includes $p + 1$-derivatives; compare [17], Theorem 1.2 and Theorem 1.5. Therefore, **(G4b)** follows immediately from Appendix A.4. if f has $\mathcal{C}^4$ sample paths and **(G2)** is replaced by their slightly stronger nondegeneracy condition.

2.2. *LKCs as projections of the EC curve.* Consider the Hilbert space with inner product

$$(3) \qquad \langle g, h \rangle = \int_{-\infty}^{\infty} g(u)h(u)e^{u^2/2}\,du,$$

consisting of all functions g, h such that $|g|^2 = \langle g, g \rangle < \infty$ and $|h|^2 = \langle h, h \rangle < \infty$. The key observation for estimation of LKCs is that the EC densities (2) are orthogonal, that is,

$$(4) \qquad \langle \rho_d, \rho_{d'} \rangle = \int_{-\infty}^{\infty} \rho_d(u)\rho_{d'}(u)e^{u^2/2}\,du = (2\pi)^{-(d+1/2)}(d-1)!\delta_{dd'},$$

where $\delta_{dd'}$ is the Kronecker delta. This follows from the orthogonality of the Hermite polynomials in the L^2 space with weights $e^{-u^2/2}$, that is,

$$(5) \qquad \int_{-\infty}^{\infty} H_{d-1}(u)H_{d'-1}(u)e^{-u^2/2}\,du = \sqrt{2\pi}(d-1)!\delta_{dd'}, \quad d, d' \in \{1, \ldots, D\}.$$

Thus, (1) implies that the LKCs can be obtained from the EEC as projection coefficients,

$$(6) \qquad \mathcal{L}_d = \frac{\langle \mathrm{EEC}^\circ, \rho_d \rangle}{|\rho_d|^2} = \frac{(2\pi)^{d/2}}{(d-1)!} \int_{-\infty}^{\infty} H_{d-1}(u)\,\mathrm{EEC}^\circ(u)\,du,$$

where $\mathrm{EEC}^\circ = \mathrm{EEC} - \mathcal{L}_0\Phi^+$ is the "pinned" EEC with $\mathcal{L}_0 = \chi(S)$. It is pinned in the sense that it tends to 0 for both small and large u, since $\lim_{u\to\infty} \mathrm{EEC}(u) = 0$ and $\lim_{u\to-\infty} \mathrm{EEC}(u) = \mathcal{L}_0$.

2.3. *Estimation of the LKCs from a single observation.* Because $\mathcal{L}_0$ is the EC of the domain S of the Gaussian random field f, it is known and need not be estimated. Given a realization of f and its empirical EC curve $u \mapsto \chi_f(u)$, which is formed by the EC of the excursion sets $A_f(u)$ of f above u, we define the corresponding "pinned" EC curve as

$$(7) \qquad \chi_f^\circ : \mathbb{R} \to \mathbb{R}, \qquad u \mapsto \chi_f(u) - \mathcal{L}_0\Phi^+(u),$$

which satisfies $\lim_{u\to\infty} \chi_f(u) = 0$ and $\lim_{u\to-\infty} \chi_f(u) = \mathcal{L}_0$. Applying the projection from (6) to χ_f° yields the estimator

$$(8) \qquad \hat{\mathcal{L}}_d = \frac{(2\pi)^{d/2}}{(d-1)!} \int_{-\infty}^{\infty} H_{d-1}(u)\chi_f^\circ(u)\,du,$$

which we call the *Hermite projection estimator* (HPE) of the LKC $\mathcal{L}_d$. The integral in (8) is well defined, since χ_f° is exponentially decaying outside the interval $[u_0, u_M]$ and is bounded on it. Comparing with (6), the estimator $\hat{\mathcal{L}}_d$ plays the role of the "observed" LKC of order d of the field f. In some sense, the HPE can be seen as a continuous version of Adler's LKC regression; compare the supplementary material Appendix A.1.

2.4. *An alternative representation.* Morse functions play a central role in the computation of the EC of a set. This is due to Morse's theorem, which computes the EC from Morse indices at critical points of a Morse function. The most general version of this result is due to Goresky and MacPherson and allows S to be a regular stratified manifold [5], Chapter 9.2.3 and Theorem 9.3.2. For regular stratified manifolds, the notion of a critical point needs to be slightly extended. A point $s \in S$ lying in the d-dimensional stratum $\partial_d S$, $d \leq D$ is called a critical point of f if the gradient of f with respect to $\tilde{S}$ at s is orthogonal to the tangent space of $\partial_d S$ at s, that is, it is a critical point of the restriction of f to $\partial_d S$. Note that manifolds with boundaries, which we consider in this work for S, are a special case of locally convex, regular stratified manifolds which have only two strata $\partial_D S$, the interior of S and $\partial_{D-1} S$ the boundary of S. A short self-contained discussion elaborating on this definition and the set of critical points of stratified manifolds can be found in [12]; a more comprehensive one in [18].

Under the assumption that the sample paths of f are almost surely Morse functions (e.g., under **(G1)**–**(G3)**), we have by Corollary 9.3.5 from [5] that the empirical EC curve, if the critical values are ordered by height, is constant between consecutive critical values. Hence, we can rewrite the empirical EC curve $u \mapsto \chi_f(u)$ as a step function, if we extend it to critical values by its left limit. The actual value of χ_f at a critical value is irrelevant as we are only interested in integrals of the empirical EC curve and f has only finitely many critical points on the compact set S [18], Remark p. 52, and, therefore, finitely many critical values. Therefore, the estimator (8) can be equivalently written as a polynomial function of the critical levels.

THEOREM 1. *Let the paths of f be almost surely Morse functions with random critical values* $\min f = u_0 < \cdots < u_M = \max f$. *Then almost surely*

$$(9) \qquad \chi_f(u) = \mathcal{L}_0 \mathbb{1}_{(-\infty, u_0]}(u) + \sum_{m=1}^{M} a_m \mathbb{1}_{(u_{m-1}, u_m]}(u)$$

with random M and random $a_m = \chi_f(u_m) \in \mathbb{Z}$, and hence

$$\hat{\mathcal{L}}_d = \frac{(2\pi)^{d/2}}{d!} \sum_{m=0}^{M} (a_m - a_{m+1}) H_d(u_m) \quad \text{with } a_0 = \mathcal{L}_0 \text{ and } a_{M+1} = 0.$$

The above representation is useful especially for numerical implementation, since it does not involve the indefinite integral (8). It reduces the estimation of LKCs to finding critical values u_m of the sample functions and the coefficient a_m. Both can be efficiently estimated; compare supplementary material Appendix A.2. In particular, this connects our estimator to works on spectral moment estimation such as [3] and [9], which derived consistent estimators from extrema of the process. Note that spectral moments and LKCs are essentially the same for stationary processes; compare [5], Section 12.5.

2.5. *Properties of the Hermite projection estimator.* Heuristically, from equations (6) and (8) by interchanging integration and expectation we obtain that $\hat{\mathcal{L}}_d$ is unbiased. Moreover, let $\hat{\mathcal{L}} = (\hat{\mathcal{L}}_1, \ldots, \hat{\mathcal{L}}_D)^{\mathrm{T}}$ be the vector of observed LKCs and denote its covariance matrix by $\Sigma = \mathrm{Cov}[\hat{\mathcal{L}}]$. Again changing order of integration and expectation yields that the (d, d')-entry $\sigma_{dd'}$ of the covariance matrix Σ can be expressed as

$$(10) \qquad \sigma_{dd'} = \frac{(2\pi)^{d/2}(2\pi)^{d'/2}}{(d-1)!(d'-1)!} \iint H_{d-1}(u) H_{d'-1}(v) \, \mathrm{Cov}[\chi_f(u), \chi_f(v)] \, du \, dv$$

using equation (8). The next theorem justifies that Fubini's theorem can be applied under the condition **(G4)**.

THEOREM 2. *Assume that f satisfies* (G1)–(G3).

(i) *Assume* (G4a), *then the HPEs are unbiased, that is,* $\mathbb{E}[\hat{\mathcal{L}}_d] = \mathcal{L}_d$ *for all* $d \in \{1, \ldots, D\}$.

(ii) *Assume* (G4b), *then* $\sigma_{dd'} = \mathrm{Cov}[\hat{\mathcal{L}}_d, \hat{\mathcal{L}}_{d'}]$ *is finite for all* $d, d' \in \{1, \ldots, D\}$. *In particular, this implies that* (10) *holds and is finite.*

A slight variation of the proof of Theorem 2(ii) allows to shed some light on the behavior of the covariance function of the EC of excursion sets of Gaussian random fields. The basic observation is that the same proof, which shows that (10) is finite for $d, d' \le D$ can also be utilized to establish that (10) is finite even if $d, d' > D$ if we strengthen (G4) slightly such that the condition hold for all $D \in \mathbb{N}$. The latter is easily satisfied under certain moment conditions as explained in Remark 3 and Appendix A.4.

COROLLARY 1. *Under the assumptions of Theorem 2(ii), if we assume that* (G4) *holds for all* $D \in \mathbb{N}$, *then we have that* $|\mathrm{Cov}[\chi_f(u), \chi_f(u')]|$ *decays faster than any polynomial in* u, u' *as* $u, u' \to \pm\infty$.

2.6. *Estimation of the LKCs from repeated observations.* Let $f_1, \ldots, f_N \sim f$ be i.i.d. random fields over the domain S with unknown covariance function satisfying (G1)–(G3) and let $\mathcal{L} = (\mathcal{L}_1, \ldots, \mathcal{L}_D)^{\mathrm{T}}$ be the vector of true LKCs. Then each EC curve χ_{f_n} yields a vector of LKC estimates $\hat{\mathcal{L}}_n = (\hat{\mathcal{L}}_{1n}, \ldots, \hat{\mathcal{L}}_{Dn})^{\mathrm{T}}$. The average estimator is defined by

$$(11) \qquad \hat{\mathcal{L}}^{(N)} = \left(\hat{\mathcal{L}}_1^{(N)}, \ldots, \hat{\mathcal{L}}_D^{(N)}\right)^{\mathrm{T}} = \frac{1}{N} \sum_{n=1}^{N} \hat{\mathcal{L}}_n.$$

Applying the strong law of large numbers (SLLN) and the standard multivariate central limit theorem (CLT), an immediate consequence of Theorem 2 is that the HPEs are unbiased and consistent estimators, which also fulfill a CLT.

COROLLARY 2. *Assume that f satisfies* (G1)–(G3).

(i) *Assume* (G4a), *then* $\hat{\mathcal{L}}^{(N)}$ *is unbiased and* $\hat{\mathcal{L}}^{(N)} \xrightarrow{a.s.} \mathcal{L}$, *as* $N \to \infty$.

(ii) *Assume* (G4b), *then* $\sqrt{N}(\hat{\mathcal{L}}^{(N)} - \mathcal{L}) \xrightarrow{D} \mathcal{N}(0, \boldsymbol{\Sigma})$ *with* $\boldsymbol{\Sigma}$ *given in* (10).

With repeated observations, the covariance matrix $\boldsymbol{\Sigma}$ can be estimated unbiasedly and consistently from the sample $f_1, \ldots, f_N \sim f$, if $N \ge 2$, via

$$(12) \qquad \hat{\boldsymbol{\Sigma}}^{(N)} = \frac{1}{N-1} \sum_{n=1}^{N} \left[\hat{\mathcal{L}}_n - \hat{\mathcal{L}}^{(N)}\right]\left[\hat{\mathcal{L}}_n - \hat{\mathcal{L}}^{(N)}\right]^{\mathrm{T}}.$$

3. LKC estimation from non-Gaussian fields. The previously developed theory relies heavily on the assumption that f is zero-mean, unit-variance and Gaussian. In applications, these assumptions usually are satisfied for a zero-mean, unit-variance limiting field G with covariance function $\mathfrak{r}$ from a fCLT, yet not for the observed fields. This is, for example, often the case in neuroimaging data; compare Appendix C.

Furthermore, our simulations in Section 5 show that even for an i.i.d. sample $f_1, \ldots, f_N \sim f$ with f Gaussian, the LKC estimation of the unit-variance process $f/\sqrt{\mathrm{Var}[f]}$ with covariance function $\mathfrak{r}$ using the HPE is biased for finite N if the mean and variance of f are unknown. This occurs because we need to use the standardized residuals

$$(13) \qquad R_n = \frac{f_n - \bar{f}}{\sqrt{N^{-1} \sum_{n=1}^{N} (f_n - \bar{f})^2}}, \quad n \in \{1, \ldots, N\}, \ N \ge 2,$$

in the HPE (8) instead of the Gaussian observations $f_1, \ldots, f_N$. Since the fields R_n, $n \in \{1, \ldots, N\}$ are non-Gaussian, the HPE is often biased.

These examples demonstrate that the HPE is only useful if we modify it so that the LKCs of a zero-mean, unit-variance Gaussian field G with covariance function $\mathfrak{r}$ can be estimated from non-Gaussian observations. To achieve this, we introduce the bootstrapped Hermite Projection Estimator (bHPE). Here, the key observation is that the LKCs of G depend solely on the derivatives of $\mathfrak{r}$, compare [5], Definition 10.7.2 and equation (12.2.4). From now on, $\mathcal{L}(\mathfrak{q})$ will denote the vector of the LKCs of a random field having correlation $\mathfrak{q}$.

Assume $R_1, \ldots, R_N$ is a sample of possible non-Gaussian fields (e.g., the standardized residuals) such that their sample covariance function $\hat{\mathfrak{r}}^{(N)}$ converges to $\mathfrak{r}$. The idea of the bHPE is to use the Gaussian multiplier bootstrap to generate from the zero-mean Gaussian field having the covariance function $\hat{\mathfrak{r}}^{(N)}$ and apply the HPE to this sample. Since for fixed observations $R_1, \ldots, R_N$, the sample generated by the multiplier bootstrap is drawn from a zero-mean, unit-variance Gaussian field, Corollary 2 implies that the resulting estimator converges almost surely to $\mathcal{L}(\hat{\mathfrak{r}}^{(N)})$ if the number of bootstrap replicates converges to infinity. To justify this approximation, we prove in Theorem 3 that $\mathcal{L}(\hat{\mathfrak{r}}^{(N)})$ is a consistent estimator of $\mathcal{L}(\mathfrak{r})$ under mild assumptions about the estimator $\hat{\mathfrak{r}}^{(N)}$. Our proof also shows that although we know $\hat{\mathfrak{r}}^{(N)}$ it is difficult to compute $\mathcal{L}(\hat{\mathfrak{r}}^{(N)})$ for manifolds of dimensions $D > 2$ directly from the definition of the LKCs. The bHPE circumvents this issue elegantly, because it computes $\mathcal{L}(\hat{\mathfrak{r}}^{(N)})$ from the easy to compute and implement HPE.

3.1. *Estimation of LKCs from a covariance estimator.* Assume that the Gaussian process f having the covariance function $\mathfrak{r} : \tilde{S} \times \tilde{S} \to \mathbb{R}$ fulfills Assumptions **(G1)**–**(G3)**. Define for a function $h : \tilde{S} \times \tilde{S} \to \mathbb{R}$ its coordinate representation $h^\alpha(x, y) = h(\phi_\alpha^{-1}(x), \phi_\alpha^{-1}(y))$ in a chart $\phi_\alpha : U_\alpha \to V_\alpha$ and $\partial_\beta^x h^\alpha(u, v) = \frac{\partial^K h^\alpha}{\partial x_{\beta_1} \ldots \partial x_{\beta_K}}|_{(x,y)=(u,v)}$ for a multiindex $\beta \in \mathbb{N}^K$ and all $u, v \in V_\alpha$. For an estimator $\hat{\mathfrak{r}}^{(N)} : \tilde{S} \times \tilde{S} \to \mathbb{R}$, we require the following property:

(R) For each chart (U_α, ϕ_α) in an atlas of $\tilde{S}$ the estimator $\hat{\mathfrak{r}}^{(N)} : \tilde{S} \times \tilde{S} \to \mathbb{R}$ satisfies $\partial_{\beta_1}^x \partial_{\beta_2}^y \hat{\mathfrak{r}}^{(N),\alpha}(x, x) \xrightarrow{N \to \infty} \partial_{\beta_1}^x \partial_{\beta_2}^y \mathfrak{r}^\alpha(x, x)$ uniformly almost surely (or uniformly in probability) for all $x \in V_\alpha$ and all $\beta_1, \beta_2 \in \mathbb{N}^K$ with $K \in I$ for some $I \subseteq \mathbb{N}$.

REMARK 4. The estimator $\hat{\mathfrak{r}}^{(N)}$ does not need to be a well-behaved estimator of $\mathfrak{r}$ on all of $S \times S$ to satisfy **(R)**. It only needs to be a good estimate of $\mathfrak{r}$ around the diagonal in $V_\alpha \times V_\alpha$.

THEOREM 3. *Let $S \subseteq \tilde{S}$ be a compact, orientable manifold with or without boundary. Let $\hat{\mathfrak{r}}^{(N)} : \tilde{S} \times \tilde{S} \to \mathbb{R}$ be a sequence of estimators satisfying* **(R)** *for $I = \{1, 2\}$ in all charts of a finite atlas of S. Then $\mathcal{L}(\hat{\mathfrak{r}}^{(N)}) \to \mathcal{L}(\mathfrak{r})$ almost surely (in probability) as $N \to \infty$.*

Under slightly stronger conditions than required for Theorem 3, the asymptotic variance and covariance of $\mathcal{L}_{D-1}(\hat{\mathfrak{r}}^{(N)})$ and $\mathcal{L}_D(\hat{\mathfrak{r}}^{(N)})$ can be obtained from the Delta method. The induced Riemannian metric g on S by a random field f expressed in the charts of the atlas from **(R)** is the $D \times D$ matrix $g^\alpha(x)$, $x \in V_\alpha$, with entries

$$g_{dd'}^\alpha(x) = \partial_d^x \partial_{d'}^y \mathfrak{r}^\alpha(x, x), \quad d, d' \in \{1, \ldots, D\}.$$

Recall that by the definition of charts of manifolds with boundaries for all $x \in \partial S$ there is a chart (U_α, ϕ_α) such that $g^\alpha(x)$ with the dth row and column removed is the restriction of g to ∂S in local coordinates. We require the following assumption:

(C) Assume that the estimator $\hat{g}^{(N)}$ of the Riemannian metric of g, given in local coordinates by the matrix $\hat{g}^{(N),\alpha}(x)$ with d-d'-entry $\partial_d^x \partial_{d'}^y \hat{\mathfrak{r}}^{(N),\alpha}(x,x)$, satisfies

$$\sqrt{N}\Big(\mathbf{vech}(\hat{g}^{(N),\alpha}) - \mathbf{vech}(g^\alpha)\Big) \rightsquigarrow \mathbf{vech}(\mathfrak{G}^\alpha)$$

weakly in $\mathcal{C}(K)^{\frac{D(D+1)}{2}}$ for all charts (U_α, ϕ_α), all compact $K \subseteq V_\alpha$ and zero-mean Gaussian processes $\mathbf{vech}(\mathfrak{G}^\alpha)$ with sample paths in $\mathcal{C}(K)^{\frac{D(D+1)}{2}}$.

REMARK 5. If $\hat{g}^{(N),\alpha}$ is derived from the sample covariance matrix of the gradient in local coordinates of $f_1, \ldots, f_N \sim f$, then assuming, for example, Lipschitz continuity of the partial derivatives of f in local coordinates such that the Lipschitz constants have finite fourth moment is enough to ensure **(R)**; compare [39].

REMARK 6. Assumption **(C)** together with the continuous mapping Theorem and the observation that $\hat{g}^{(N)}$ and g are a symmetric, covariant 2-tensor field on $\tilde{S}$ implies that for any two charts (U_ϕ, ϕ), (U_ψ, ψ) and any $s \in S$ with $s = \phi^{-1}(x) = \psi^{-1}(\tilde{x}) \in U_\phi \cap U_\psi$ and $x \in V_\phi$, $\tilde{x} \in V_\psi$ there exists an invertible matrix $D_{\phi,\psi,x}$ such that

$$\hat{g}^{(N),\phi}(x) = D_{\phi,\psi,x}^T \hat{g}^{(N),\psi}(\tilde{x}) D_{\phi,\psi,x}, \qquad g^\phi(x) = D_{\phi,\psi,x}^T g^\psi(\tilde{x}) D_{\phi,\psi,x},$$

$$\mathfrak{G}^\phi(x) = D_{\phi,\psi,x}^T \mathfrak{G}^\psi(\tilde{x}) D_{\phi,\psi,x}.$$

PROPOSITION 1. *Let S be an orientable, compact manifold with our without boundary, $\mathcal{H}_{D-1}^g(ds)$ denote the volume form of ∂S with respect to g and assume that the estimator $\hat{g}^{(N)}$ satisfies* **(C)**, *then*

$$\sqrt{N}\left(\begin{pmatrix} \mathcal{L}_{D-1}(\hat{g}^{(N)}) \\ \mathcal{L}_D(\hat{g}^{(N)}) \end{pmatrix} - \begin{pmatrix} \mathcal{L}_{D-1}(g) \\ \mathcal{L}_D(g) \end{pmatrix}\right) \rightsquigarrow \begin{pmatrix} \int_{\partial S} \frac{1}{4} \mathrm{tr}[g_s^{-1}\mathfrak{G}_s] \mathcal{H}_{D-1}^g(ds) \\ \int_S \frac{1}{2} \mathrm{tr}[g_s^{-1}\mathfrak{G}_s] \mathcal{H}_D^g(ds) \end{pmatrix}.$$

Recall that for manifolds without boundary $\mathcal{L}_{D-1} = 0$ (see [5], Theorem 12.4.1) such that only the second component of the above vector is used in this case and that the integral on manifolds is defined by using local coordinates and a partition of unity. The latter is explicitly carried out in the proof of this result.

From the above result, we obtain the asymptotic covariances of the estimators of the highest two LKCs:

$$\mathrm{Var}[\mathcal{L}_{D-1}(\hat{g}^{(N)})] = \frac{1}{16} \int_{\partial S} \int_{\partial S} \mathbb{E}[\mathrm{tr}[g_s^{-1}\mathfrak{G}_s] \mathrm{tr}[g_t^{-1}\mathfrak{G}_t]] \mathcal{H}_{D-1}^g(ds)\mathcal{H}_{D-1}^g(dt),$$

$$\mathrm{Cov}[\mathcal{L}_{D-1}(\hat{g}^{(N)}), \mathcal{L}_D(\hat{g}^{(N)})] = \frac{1}{8} \int_S \int_{\partial S} \mathbb{E}[\mathrm{tr}[g_s^{-1}\mathfrak{G}_s] \mathrm{tr}[g_t^{-1}\mathfrak{G}_t]] \mathcal{H}_{D-1}^g(ds)\mathcal{H}_D^g(dt),$$

$$\mathrm{Var}[\mathcal{L}_D(\hat{g}^{(N)})] = \frac{1}{4} \int_S \int_S \mathbb{E}[\mathrm{tr}[g_s^{-1}\mathfrak{G}_s] \mathrm{tr}[g_t^{-1}\mathfrak{G}_t]] \mathcal{H}_D^g(ds)\mathcal{H}_D^g(dt).$$

Interchanging the integral and expectation is justified as $\mathfrak{G}$ is a Gaussian process with continuous sample paths and, therefore, the above integrals with absolute values inside the expectations exist and are integrable as ∂S and S are compact and, therefore, the involved partition of unity is finite. Unfortunately, these expressions are in general hard to evaluate explicitly.

3.2. *Bootstrapped Hermite projection estimator.* Let $R_1, R_2, \ldots, R_N$ be random fields over $\tilde{S}$ with almost surely $\mathcal{C}^2$-sample paths and $(\Omega, \mathbb{P})$ be the underlying probability space. The empirical covariance function is

$$\hat{\mathfrak{r}}^{(N)}(s, s') = N^{-1} \sum_{n=1}^{N} R_n(s) R_n(s') \quad \text{for } s, s' \in \tilde{S}.$$

We denote with $R_{n\omega}$ and $\hat{\mathfrak{r}}_{\omega}^{(N)}$ realizations of R_n and $\hat{\mathfrak{r}}^{(N)}$ for $\omega \in \Omega$. In order to calculate $\mathcal{L}(\hat{\mathfrak{r}}_{\omega}^{(N)})$ using the HPE, we define the Gaussian multiplier field.

DEFINITION 1 (Gaussian multiplier field). For each $\omega \in \Omega$, define the *Gaussian multiplier field* (GMF) by

(14) $$R_{\mathbf{g}\omega}^{(N)} = \frac{1}{\sqrt{N}} \sum_{n=1}^{N} g_n R_{n\omega},$$

where $\mathbf{g} = (g_1, \ldots, g_N)$ with $g_1, \ldots, g_N \sim \mathcal{N}(0, 1)$ i.i.d. defined over a probability space $(\tilde{\Omega}, \tilde{\mathbb{P}})$.

For each $\omega \in \Omega$ and $N \in \mathbb{N}$, the GMF is a Gaussian field over $\tilde{S}$ with mean and covariance function

$$\mathbb{E}[R_{\mathbf{g}\omega}^{(N)}(s)] = 0, \qquad \mathbb{E}[R_{\mathbf{g}\omega}^{(N)}(s) R_{\mathbf{g}\omega}^{(N)}(s')] = \hat{\mathfrak{r}}_{\omega}^{(N)}(s, s'), \quad s, s' \in \tilde{S}.$$

Moreover, for large enough N the GMF satisfies **(G1)--(G3)** for almost all $\omega \in \Omega$ assuming **(R)** with $I = \{0, 1, 2\}$ and the following condition:

(H) For the charts from **(R)**, the sample paths $\partial_\beta R_n^\alpha$, $|\beta| = 2$, are almost surely γ-Hölder continuous for $\gamma \in (0, 1)$ and all $n \in \{1, \ldots, N\}$.

The proof can be found in Lemma 6 in the supplementary material. Hence, if the GMF satisfies **(G4a)**, then the conditions of Corollary 2(i) are satisfiedm which means that the HPE $\hat{\mathcal{L}}(R_{\mathbf{g}\omega}^{(N)})$ is an unbiased estimate of $\mathcal{L}(\hat{\mathfrak{r}}^{(N)})$. Thus, we define the *bootstrapped Hermite projection estimator* (bHPE) for fixed $\omega \in \Omega$ as

(15) $$\hat{\mathcal{L}}_{B\omega}^{(N)} = \lim_{M \to \infty} \frac{1}{M} \sum_{m=1}^{M} \hat{\mathcal{L}}(R_{\mathbf{g}_m\omega}^{(N)}),$$

where $R_{\mathbf{g}_1\omega}^{(N)}, R_{\mathbf{g}_2\omega}^{(N)} \ldots \sim R_{\mathbf{g}\omega}^{(N)}$ is an i.i.d. sequence of the GMF. By the SLLN, this estimator is $\tilde{\Omega}$-almost surely identical to $\mathcal{L}(\hat{\mathfrak{r}}_{\omega}^{(N)})$. Therefore, a Monte Carlo simulation based on the HPE for given residuals $R_{1\omega}, \ldots, R_{N\omega}$ can be used to approximate the otherwise hard to compute $\mathcal{L}(\hat{\mathfrak{r}}_{\omega}^{(N)})$.

REMARK 7. In the setting that $f_1, \ldots, f_N \sim f$ are i.i.d. with correlation function $\mathfrak{r}$, simple conditions, such that $\sqrt{N}(\bar{f} - \mathbb{E}[f])/\sqrt{\text{Var}[f]}$ converges weakly in $\mathcal{C}(S)$ to a zero-mean Gaussian field G with covariance function $\mathfrak{r}$ and that the GMF obtained from the standardized residuals defined in (13) fulfills **(R)** with $I = \{0, 1, 2\}$ and **(H)**, are given in Appendix A.7.

4. Estimation of the EEC and applications. We only present the results of EEC estimation for Gaussian fields. Nevertheless, most of the following results can be easily extended to Gaussian-related fields as introduced in [34].

4.1. *Plug-in estimation of the EEC.* In this section, we assume that $\hat{\mathcal{L}}^{(N)}$ is an arbitrary estimator of the LKCs $\mathcal{L}$. Given these estimates [4] suggested the plug-in estimator into the GKF, that is,

$$(16) \qquad \widehat{\mathrm{EEC}}^{(N)}(u) = \mathcal{L}_0 \Phi^+(u) + \sum_{d=1}^{D} \hat{\mathcal{L}}_d^{(N)} \rho_d(u),$$

to obtain a smooth estimate of the EEC. By linearity, this plug-in estimator is unbiased for the EEC if $\hat{\mathcal{L}}^{(N)}$ is unbiased, and its covariance function is

$$(17) \qquad C(u, v) = \sum_{d=1}^{D} \sum_{d'=1}^{D} \sigma_{dd'}^{(N)} \rho_d(u) \rho_{d'}(v),$$

where $\sigma_{dd'}^{(N)}$ is the (d, d') entry of the covariance matrix $\mathbf{\Sigma}^{(N)}$ of the vector $\hat{\mathcal{L}}^{(N)}$. The latter is well defined only if $\mathbf{\Sigma}^{(N)}$ exists. Consistency and a fCLT for the $\widehat{\mathrm{EEC}}^{(N)}$ can be derived from corresponding properties of the estimator $\hat{\mathcal{L}}^{(N)}$.

PROPOSITION 2. *The plug-in estimate of the EEC has the following properties*:

(i) *Assume that $\hat{\mathcal{L}}^{(N)}$ is consistent. Then $\widehat{\mathrm{EEC}}^{(N)}$ and $\frac{d^k}{du^k}\widehat{\mathrm{EEC}}^{(N)}$, $k \geq 1$, are uniformly consistent estimators of the* EEC *and $\frac{d^k}{du^k}$* EEC, *respectively.*

(ii) *Assume that $\sqrt{N}(\hat{\mathcal{L}}^{(N)} - \mathcal{L}) \xrightarrow{D} \mathcal{N}(0, \mathbf{\Sigma})$. Then the estimator $\widehat{\mathrm{EEC}}^{(N)}$ satisfies a fCLT in $\mathcal{C}_b(\mathbb{R})$, the Banach space of bounded and continuous functions over $\mathbb{R}$, that is,*

$$(18) \qquad \sqrt{N}\Big[\widehat{\mathrm{EEC}}^{(N)}(u) - \mathrm{EEC}(u)\Big] \xrightarrow{D} G(u) = \sum_{d=1}^{D} Z_d \rho_d(u), \quad N \to \infty.$$

Here, $(Z_1, \ldots, Z_D)$ is a Gaussian random vector with zero-mean and covariance $\mathbf{\Sigma}$.

REMARK 8. The above theorem can be generalized to the expected Euler characteristic curves of Gaussian related fields as they satisfy a Gaussian kinematic formula; see [34].

The fCLT (18) for $\widehat{\mathrm{EEC}}^{(N)}$ allows constructing confidence bands for the EEC. In particular, asymptotic two-sided $(1 - \alpha)$-pointwise confidence bands can be built as

$$(19) \qquad \widehat{\mathrm{EEC}}^{(N)}(u) \pm t_{N-1, 1-\alpha/2} \sqrt{\hat{C}(u, u)/N},$$

where the estimate of the variance function $\hat{C}(u, u)$ is obtained as a plug-in estimator substituting the sample covariance $\hat{\mathbf{\Sigma}}^{(N)}$ given in (12) into (17). Here, $t_{N-1, 1-\alpha/2}$ is the $1 - \alpha/2$ quantile of Student's t-distribution with $N - 1$ degrees of freedom. In the simulations in Section 5, it is shown that the confidence bands (19) are tighter and have better coverage than the pointwise confidence bands based on the pointwise CLT for the sample average $\bar{\chi}^{(N)}$, that is,

$$(20) \qquad \bar{\chi}^{(N)}(u) \pm t_{N-1, 1-\alpha/2} \sqrt{\widehat{\mathrm{Var}}[\chi_f(u)]/N},$$

where $\widehat{\mathrm{Var}}[\chi_f(u)]$ is the sample variance of $\chi_{f_1}(u), \ldots, \chi_{f_N}(u)$.

Proposition 2 even allows constructing simultaneous confidence bands. Assume that $\mathbf{\Sigma}$ is positive definite. Then the process $G(u)/\sqrt{C(u, u)}$ has sample paths in $\mathcal{C}_b(\mathbb{R})$ because for all $u \in \mathbb{R}$ we have that

$$\left| \frac{G(u)}{\sqrt{C(u, u)}} \right| \leq \frac{\|(Z_1, \ldots, Z_D)\|}{\lambda_{\min}},$$

where Z_d, G, C and $\boldsymbol{\Sigma}$ are defined in Proposition 2 and $\lambda_{\min}$ being the smallest eigenvalue of $\boldsymbol{\Sigma}$. This can also be derived from noting that

$$(21) \qquad \lim_{u \to \pm\infty} \frac{\rho_k(u)}{\sqrt{\sum_{d=1}^D \sum_{d'=1}^D \sigma_{dd'} \rho_d(u) \rho_{d'}(u)}} = \begin{cases} \dfrac{(\pm 1)^D}{\sqrt{\sigma_{DD}}} & \text{for } k = D, \\ 0 & \text{else.} \end{cases}$$

Thus, a standard argument using Slutzky's lemma, for example, [13, 38], yields that the intervals with endpoints

$$(22) \qquad \widehat{\mathrm{EEC}}^{(N)}(u) \pm q_{1-\alpha} \sqrt{\frac{\hat{C}(u,u)}{N}},$$

form a simultaneous $(1-\alpha)$-confidence band for the EEC if

$$\mathbb{P}\left[\max_{u \in \mathbb{R}} \left| \frac{G(u)}{\sqrt{C(u,u)}} \right| > q_{1-\alpha} \right] \geq 1 - \alpha.$$

A simple estimate of $q_{1-\alpha}$ leading to conservative, simultaneous $(1-\alpha)$-confidence bands can be obtained from a Monte Carlo simulation using zero-mean Gaussian random vectors $(\hat{Z}_1, \ldots, \hat{Z}_D)$ with covariance $\hat{\boldsymbol{\Sigma}}^{(N)}$ by finding the $1 - \alpha$ quantile of $\|(Z_1, \ldots, Z_D)\|/\hat{\lambda}_{\min}$, where $\hat{\lambda}_{\min}$ denotes the smallest eigenvalue of $\hat{\boldsymbol{\Sigma}}^{(N)}$.

However, (21) suggests that the above estimate can be improved, although the maximum is over $\mathbb{R}$. In fact, for $D \in \{1, 2\}$ we can analytically compute the critical quantile. For $D = 1$, it holds for all $u \in \mathbb{R}$ that

$$\max_{u \in \mathbb{R}} \frac{G(u)}{\sqrt{C(u,u)}} = \max_{u \in \mathbb{R}} \frac{Z_1 \rho_1(u)}{\sqrt{\rho_1^2(u)\sigma_{11}}} = \frac{Z_1}{\sqrt{\sigma_{11}}} \sim \mathcal{N}(0,1),$$

which implies that the confidence band (19) is a simultaneous confidence band. Similarly, the global maximum of $|G(u)/\sqrt{C(u,u)}|$ over $\mathbb{R}$ can be analytically derived for $D = 2$ as shown in the next proposition.

PROPOSITION 3. *Let $D = 2$ and $\boldsymbol{\Sigma}$ given in* (10) *be positive definite and let* $\mathbf{Z} = (Z_1, Z_2)^T \sim \mathcal{N}(0, \boldsymbol{\Sigma})$. *Then*

$$\max_{u \in \mathbb{R}} \left| \frac{G(u)}{\sqrt{C(u,u)}} \right| = \sqrt{\mathbf{Z}^T \boldsymbol{\Sigma}^{-1} \mathbf{Z}} \, \mathbb{1}_{\{\sigma_{22} Z_1 - \sigma_{12} Z_2 \neq 0\}} + \frac{|Z_1|}{\sqrt{\sigma_{11}}} \mathbb{1}_{\{\sigma_{22} Z_1 - \sigma_{12} Z_2 = 0\}}.$$

Here, $\mathbb{1}_A$ denotes the characteristic function of the set A.

The main importance of Proposition 3 is that the asymptotical correct quantile $q_{1-\alpha}$ in (22) for $D = 2$ is the $1 - \alpha$ quantile of the χ-distribution with two degrees of freedom since $\mathbb{P}[\sigma_{22} Z_1 = \sigma_{12} Z_2] = 0$. As before, however, the variance $C(u,u)$ is usually unknown and we therefore replaced it by the estimate $\hat{C}(u,u)$. Thus, a better choice of the quantile $q_{1-\alpha}$ for practical purposes is the square root of the $1 - \alpha/2$ quantile of the Hotelling's $T_{2,N-1}^2$ distribution because $\mathbf{Z}^T \hat{\boldsymbol{\Sigma}}^{-1} \mathbf{Z}$ is approximately Hotelling's $T_{2,N-1}^2$ distributed. The performance of these simultaneous confidence bands for the HPE and bHPE are demonstrated in Section 5.

4.2. *Hermite projection estimator of the EEC.* Consider the EEC plug-in estimator (16) using the HPE (or bHPE) of the LKCs from Section 2.6. With some abuse of nomenclature, we call this the *(bootstrapped) Hermite projection estimator* of the EEC since they are projections onto the subspace spanned by the EC densities $\rho_1, \ldots, \rho_D$ with respect to the Hilbert space structure introduced in Section 2.2.

Let $f_1, \ldots, f_N \sim f$ be i.i.d. zero-mean, unit-variance Gaussian fields satisfying **(G1)**–**(G4)**. Thus, the HPE of the EEC satisfies Proposition 2. Moreover, each HPE $(\hat{\mathcal{L}}_{1n}, \ldots, \hat{\mathcal{L}}_{Dn})$ of LKCs from an observation f_n yields a smooth estimate of the EEC as a linear combination of the EC densities via

$$\hat{\chi}_{f_n}(u) = \mathcal{L}_0 \Phi^+(u) + \sum_{d=1}^{D} \hat{\mathcal{L}}_{dn} \rho_d(u).$$

By linearity, we can write the plug-in EEC estimator using the HPE of the LKCs as the average of these smoothed EC curves, that is,

$$(23) \qquad \widehat{\mathrm{EEC}}^{(N)}(u) = \mathcal{L}_0 \Phi^+(u) + \sum_{d=1}^{D} \hat{\mathcal{L}}_d^{(N)} \rho_d(u) = \frac{1}{N} \sum_{n=1}^{N} \hat{\chi}_{f_n}(u).$$

An alternative estimate of the EEC is the sample average of the observed EC curves,

$$\bar{\chi}^{(N)}(u) = \frac{1}{N} \sum_{n=1}^{N} \chi_{f_n}(u).$$

This is an unbiased and consistent estimator satisfying pointwise a CLT, since the observed EC curves are i.i.d. and have finite variance by **(G4)**. Using linearity of (8), the HPE of LKCs (11) can also be obtained from the average EC curve via

$$(24) \qquad \hat{\mathcal{L}}_d^{(N)} = \frac{(2\pi)^{d/2}}{(d-1)!} \int_{-\infty}^{\infty} H_{d-1}(u) \big(\bar{\chi}^{(N)}(u) - \mathcal{L}_0 \Phi^+(u)\big)\, du.$$

Plugging this into (23) and using (8) yields

$$(25) \qquad \widehat{\mathrm{EEC}}^{(N)}(u) = \mathcal{L}_0 \Phi^+(u) + \sum_{d=1}^{D} \frac{\langle \bar{\chi}^{(N)}(u) - \mathcal{L}_0 \Phi^+(u), \rho_d \rangle}{|\rho_d|^2} \rho_d(u).$$

Thus, $\widehat{\mathrm{EEC}}^{(N)}$ is the orthogonal projection of $\bar{\chi}^{(N)}(u)$ onto the vector space spanned by the EC densities according to the inner product (3), explaining the name HPE.

4.3. *Inference based on the estimated EEC.* The estimated EEC can be used for statistical inference by finding a threshold u such that $\widehat{\mathrm{EEC}}(u)$ is less or equal to a prespecified value α. Because minima and maxima of Morse functions locally behave like quadrics [25], Lemma 2.2, and have no accumulation points if their domain is compact [25], Corollary 2.3, it follows that the Euler characteristic of the excursion set for large enough u is essentially counting simply connected components above u. If there is just one connected component or no connected component, then the EC is either 0 or 1, respectively. Thus, this heuristic suggests that for large enough u the EEC should approximate the FWER of voxelwise given test statistics $T(s)$, $s \in S$, on an image S. This was the pioneering approach taken by Keith Worsley in the analysis of brain images, for example, [41, 42]. This approach is called the *Euler characteristic heuristic*. More precisely, it states that for Gaussian related fields T and high enough threshold u the probability of the maximum of T being larger than u is well approximated by the EEC of the excursions set above u, that is,

$$\mathrm{FWER}(u) = \mathbb{P}\Big\{ \sup_{s \in S} T(s) > u \Big\} \approx \mathrm{EEC}(u).$$

This approximation typically works well, if u_α satisfies $\mathrm{EEC}(u_\alpha) = \alpha$ with $\alpha \leq 0.05$. In the case of T being a zero-mean, unit-variance Gaussian field, the quality of this approximation has been studied in [33] where it has been shown that the difference between the EEC and the FWER decreases exponentially in u^2.

Another interpretation of thresholding the EEC at level α is the following. For high but somewhat lower thresholds u than for FWER control, the Euler characteristic of the excursion set is essentially the number of connected components (or clusters) above u. This suggests that the EEC approximates the cluster error rate (CER), defined as the expected number of connected components in the excursion set $A_T(u)$, that is,

$$(26) \qquad \text{CER}(u) = \mathbb{E}[\#\text{connected components of } A_T(u)] \approx \text{EEC}(u).$$

Hence, finding c_α such that $\text{EEC}(c_\alpha) = \alpha$ controls the CER to be approximately α. Although uncommon, this approach has been used in neuroimaging with $\alpha = 1$, meaning the excursion set contains on average approximately one false connected component; see [8].

Suppose the EEC is estimated via (25) and a significance threshold $\hat{u}_\alpha^{(N)}$ is found satisfying $\widehat{\text{EEC}}^{(N)}(\hat{u}_\alpha^{(N)}) = \alpha$. The following theorem gives the asymptotic properties of the estimated threshold, especially how variable it is. The results are valid for any EEC estimator for which the results of Proposition 2 hold, in particular the HPE. Let $\text{EEC}'(u)$ denote the derivative of the EEC, that is,

$$\text{EEC}'(u) = \sum_{d=0}^{D} \mathcal{L}_d \rho_d'(u) = -\sqrt{2\pi} \sum_{d=0}^{D} \mathcal{L}_d \rho_{d+1}(u).$$

THEOREM 4. *Assume that the results of Proposition 2 are satisfied. Then the random threshold $\hat{u}_\alpha^{(N)}$ has the following properties*:

(i) *$\hat{u}_\alpha^{(N)}$ is a consistent estimator of u_α.*
(ii) *Let α be small enough such that $\text{EEC}'(u_\alpha) \neq 0$. Then $\sqrt{N}(\hat{u}_\alpha^{(N)} - u_\alpha)$ converges in distribution to $G(u_\alpha)/\text{EEC}'(u_\alpha)$, where $G(u)$ is the Gaussian process in (18).*

A consequence of Theorem 4 is that, for large N, $\hat{u}_\alpha^{(N)}$ is approximately Gaussian with mean u_α and variance

$$(27) \qquad \text{Var}[\hat{u}_\alpha^{(N)}] = \frac{C(u_\alpha, u_\alpha)}{N[\text{EEC}'(u_\alpha)]^2},$$

where $C(u, u)$ is given by (17). In practice, we estimate this variance by substituting estimators for u_α, $C(u, u)$ and the LKCs as described above.

5. Simulation studies.

5.1. *Design of the simulations.* We compare the Hermite projection estimator (HPE) given by (11), the bootstrapped Hermite projection estimator (bHPE) from (15) using 5,000 bootstrap replicates, the warping estimator (WarpE) [35] and an estimator (IsotE) tailored to isotropic fields with the square exponential covariance function [22]. The latter is part of the software package SPM12 and frequently used in the neuroimaging community. We always use 1,000 Monte Carlo runs and consider two different scenarios for estimation of the LKCs. The *theoretical scenario* assumes that the mean and variance are known and equal to zero and one, respectively, as required for the theory presented in Section 2. The *experimental scenario* assumes that the mean and variance are unknown. Thus, standardized residuals are used as input for the estimators as discussed in Sections 3 instead of using the generated samples directly.
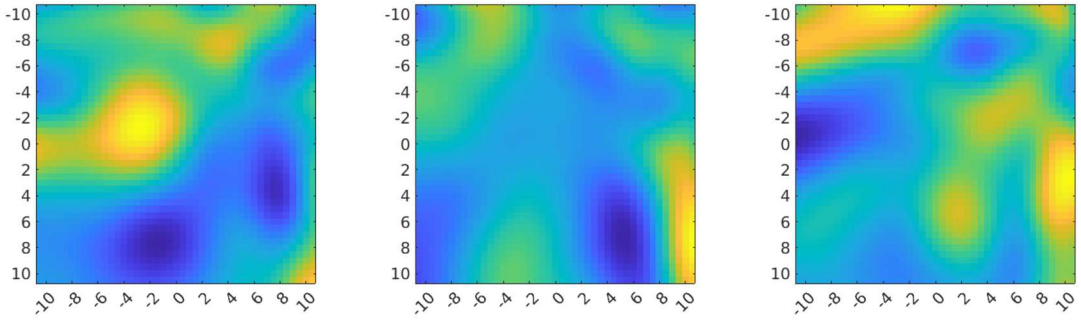
FIG. 2. *Three sample paths of the nonstationary Gaussian process given by* (31) *for* $L = 10.5$, $A = B = 2.5$ *and* $a = -b = 0.05$.

5.2. *Isotropic Gaussian and non-Gaussian fields.* A common example of an isotropic Gaussian random field is

$$(28) \qquad f(s) = \frac{\sqrt{\pi}}{v} \iint e^{-\frac{\|s-t\|^2}{2v^2}} \, dW_t \quad \text{for } s \in S = [1, L]^2,$$

where W is a Wiener field on $\mathbb{R}^2$ and the integral is interpreted as an Itô integral. Its covariance function is $C(s) = e^{-\|s\|^2/(4v^2)}$. For an isotropic field on a compact domain $S \subset \mathbb{R}^2$, the LKCs can be derived by $\mathcal{L}_0 = \mathcal{L}_0(S)$, $\mathcal{L}_1 = \lambda_2^{1/2}\mathcal{L}_1(S)$ and $\mathcal{L}_2 = \lambda_2\mathcal{L}_2(S)$, where $\mathcal{L}_0(S)$, $\mathcal{L}_1(S)$ and $\mathcal{L}_2(S)$ are the LKCs of the domain S with respect to the standard metric and λ_2 is the second spectral moment, equal to the variance of any directional derivative of f [5]. For (28), this yields $\mathcal{L}_0 = 1$, $\mathcal{L}_1 = \sqrt{2/v}(L-1)$ and $\mathcal{L}_2 = (2/v)^{-1}(L-1)^2$. Setting $v = 5$ and $L = 50$ gives $\mathcal{L}_1 = 13.86$ and $\mathcal{L}_2 = 48.02$, which are used in this simulation.

To generate an i.i.d. sample $f_1(s), \ldots, f_N(s)$ from (28), we approximate it by

$$(29) \qquad f_n(s) = \frac{\sum_{k,l=1}^{L} e^{-\frac{\|s-(k,l)\|^2}{2v^2}} W_{kl;n}}{\sum_{k,l=1}^{L} e^{-\frac{\|s-(k,l)\|^2}{v^2}}},$$

where $W_{kl;n}, k, l \in \{1, \ldots, L\}, n \in \{1, \ldots, N\}$ are i.i.d. zero-mean, unit-variance random variables. We consider a Gaussian case, where the $W_{kl;n}$ are $\mathcal{N}(0, 1)$ and a non-Gaussian case where they are $(\chi_3^2 - 3)/\sqrt{6}$. Neither the covariance function nor the LKCs depend on the distribution of $W_{kl;n}$. Hence, the LKCs of the field (29) approximate the LKCs of the field (28) for any choice of the $W_{kl;n}$, if v is large enough. This is further elaborated below.

5.3. *Nonstationary Gaussian and non-Gaussian fields.* In this section, we explain the nonstationary, Gaussian and the non-Gaussian random field f defined over $[0, 1]^2$, which we use in our simulations. The Gaussian version is defined by the following Itô integral:

$$(30) \qquad f(s) = \sqrt{\frac{\pi}{\lambda_1(s_1)\lambda_2(s_2)}} \iint e^{-\frac{1}{2}(\frac{s_1-\tau_1}{\lambda_1(s_1)})^2} e^{-\frac{1}{2}(\frac{s_2-\tau_2}{\lambda_2(s_2)})^2} \, dW_\tau,$$

for $s = (s_1, s_2) \in S = [-L, L]^2$, W is a Wiener field on $\mathbb{R}^2$ and λ_i, $i = 1, 2$, being strictly positive functions on S. Three sample paths of this field can be found in Figure 2. In order to get a non-Gaussian process, we replace the Gaussian i.i.d. random variables in simulating the process (30) by i.i.d. Student's t_3-distributed random variables.

Using a basic computation or the Itô isometry and the integral identity,

$$\int_{-\infty}^{\infty} \varphi(x)\varphi(a + bx), dx = \frac{2}{\sqrt{1+b^2}}\varphi\left(\frac{a}{\sqrt{1+b^2}}\right)$$

for the standard normal density φ and $a, b \in \mathbb{R}$, we obtain for all $s, t \in [-L, L]^2$ that

$$(31) \quad \text{Cov}[f(s), f(t)] = \frac{2\sqrt{\lambda_1(s_1)\lambda_1(t_1)\lambda_2(s_2)\lambda_2(t_2)}}{\sqrt{\lambda_1^2(s_1) + \lambda_1^2(t_1)}\sqrt{\lambda_2^2(s_2) + \lambda_2^2(t_2)}} e^{-\frac{1}{2}\frac{(s_1-t_1)^2}{\lambda_1^2(s_1)+\lambda_1^2(t_1)}} e^{-\frac{1}{2}\frac{(s_2-t_2)^2}{\lambda_2^2(s_2)+\lambda_2^2(t_2)}}.$$

Choosing $\lambda_1(s) = Ae^{as}$ and $\lambda_2(s) = Be^{bs}$, $a, b \in \mathbb{R}$, yields

$$\frac{2\sqrt{\lambda_1(s_1)\lambda_1(t_1)\lambda_2(s_2)\lambda_2(t_2)}}{\sqrt{\lambda_1^2(s_1) + \lambda_1^2(t_1)}\sqrt{\lambda_2^2(s_2) + \lambda_2^2(t_2)}} = \frac{1}{\sqrt{\cosh(a(s_1 - t_1))}\sqrt{\cosh(b(s_2 - t_2))}}.$$

Using this, we can compute the induced Riemannian metric by f on $[0, 1]^2$ by taking partial derivatives of (31) (compare [5], Section 12.2), which yields

$$g(s) = \frac{1}{2}\begin{pmatrix} a^2 + A^{-2}e^{-2as} & 0 \\ 0 & b^2 + B^{-2}e^{-2bs} \end{pmatrix}.$$

Thus, we obtain (compare [39], Section 3.2.)

$$\mathcal{L}_1 = \frac{1}{\sqrt{2}}\int_{-L}^{L}\sqrt{a^2 + A^{-2}e^{-2ax}}\,dx + \frac{1}{\sqrt{2}}\int_{-L}^{L}\sqrt{b^2 + B^{-2}e^{-2bx}}\,dx,$$

$$\mathcal{L}_2 = \frac{1}{2}\left(\int_{-L}^{L}\sqrt{a^2 + A^{-2}e^{-2ax}}\,dx\right)\left(\int_{-L}^{L}\sqrt{b^2 + B^{-2}e^{-2bx}}\,dx\right),$$

which yields $\mathcal{L}_1 \approx 12.53$ and $\mathcal{L}_2 \approx 39.25$ for $L = 10.5$, $A = B = 2.5$ and $a = -b = 0.05$.

5.4. *LKC estimation.* In the isotropic Gaussian case, Figure 3 confirms the theoretical results that the HPE and the bHPE are consistent in the theoretical scenario. For every N, the HPE is almost unbiased in the theoretical scenario, as predicted by Theorem 2(i). For small N, the residuals are not Gaussian processes in the experimental scenario causing the HPE to have a bias. The bHPE, however, is almost unbiased in the theoretical and the experimental scenario. The bHPE has a similar variance as the WarpE, which turns out to be smaller than the variance of the HPE. Unbiasedness for the WarpE is expected for standardized residuals [35]. For a fair comparison, we implemented the WarpE assuming zero-mean, unit-variance observations as described on page 917, bottom left of [35]. In this case, the WarpE seems to have a bias for small sample sizes. A keen eye will also notice a small downward bias, which seems to prevail for all compared estimators even for large N. This discrepancy is due to the fact that the simulated field (29), which is a discretized version of the theoretical field (28), has slightly different LKCs. Table 1 shows that the relative difference between the HPE and the theoretical LKCs of (28) vanishes as ν increases. This is because the number of data points inside the kernel domain makes the field less wiggly, and hence the integral in (28) is approximated better by the discretized version (29).

For isotropic non-Gaussian data, Figure 4 shows that the bHPE is still unbiased. Only the HPE cannot handle this scenario, since the EC curves are not derived from a Gaussian field. WarpE and IsotE are based on estimation of the covariance of the derivative of the random field and, therefore, are expected to still work for this particular non-Gaussian field.

The simulation results of estimation of LKCs of the nonstationary Gaussian and non-Gaussian data are shown in the Figures 5 and 6. There are only little differences between these simulations and our previous observations. The bHPE performs still well in all scenarios, while the HPE and the WarpE requires the experimental setup to be unbiased. Unlike before, the HPE and IsotE do not perform well in these simulations as they are tailored to Gaussianity and stationarity, respectively.
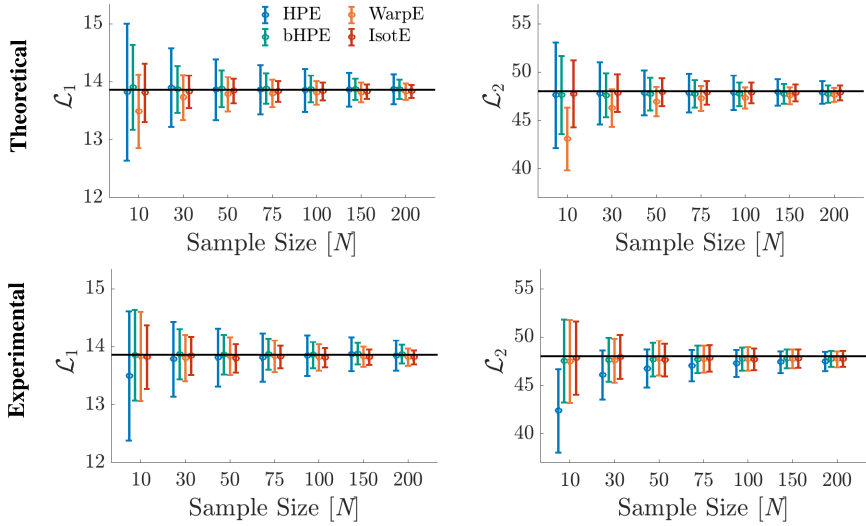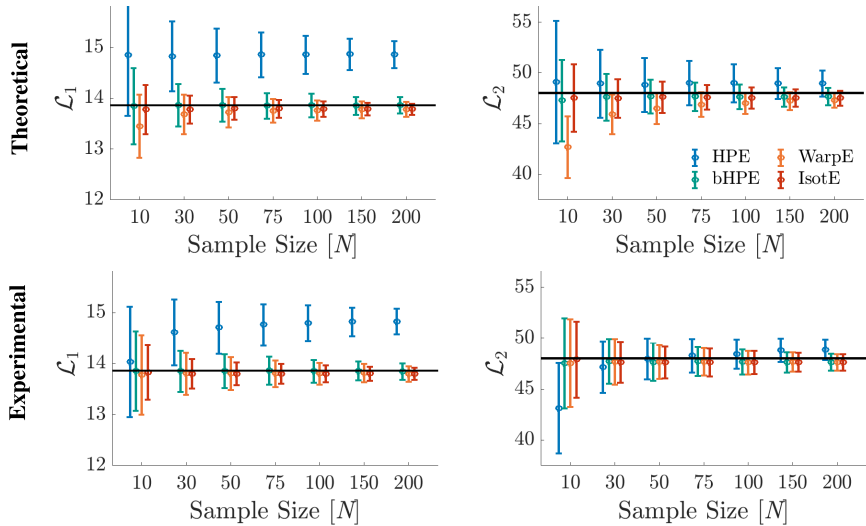
FIG. 3. *Isotropic Gaussian field ($v = 5$ and $L = 50$): comparison of mean and standard deviation of different LKC estimators. Black lines represent the theoretical LKCs.*

TABLE 1

Comparison of relative bias $\mathbb{E}[\hat{\mathcal{L}}_d - \mathcal{L}_d]/\mathcal{L}_d$ for the HPE

v	2	3	5	6	7
$\hat{\mathcal{L}}_1, N = 10$	-0.0195	-0.0179	-0.0075	-0.0025	0.0011
$\hat{\mathcal{L}}_2, N = 10$	-0.0169	-0.0090	-0.0097	-0.0069	0.0045
$\hat{\mathcal{L}}_1, N = 75$	-0.0240	-0.0121	-0.0075	-0.0047	0.0012
$\hat{\mathcal{L}}_2, N = 75$	-0.0138	-0.0076	-0.0065	-0.0065	0.0006

FIG. 4. *Isotropic non-Gaussian field ($v = 5$ and $L = 50$): comparison of mean and standard deviation of different LKC estimators. Black lines represent the theoretical LKCs.*
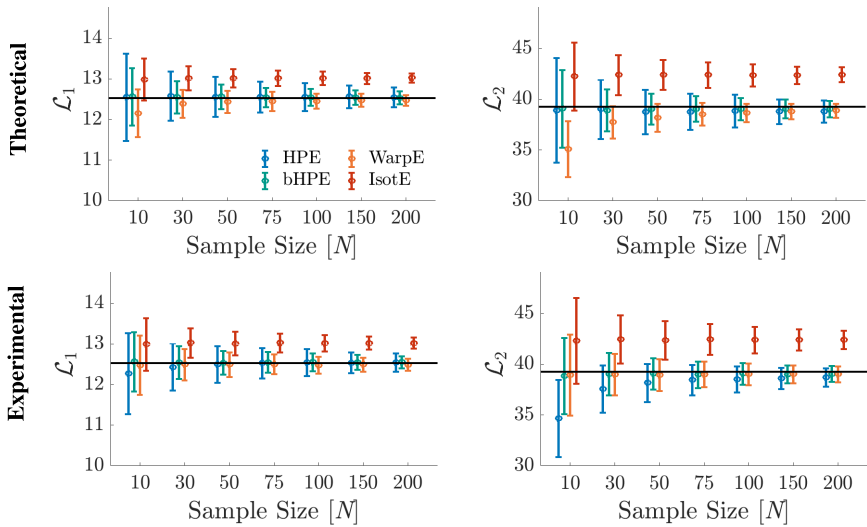
FIG. 5. *Nonstationary Gaussian field given by* (31) *for* $L = 10.5$, $A = B = 2.5$ *and* $a = -b = 0.05$: *comparison of mean and standard deviation of different LKC estimators. Black lines represent the theoretical LKCs.*

5.5. *HPE of the EEC.* Moving on to HPE estimation of the EEC, the covariance function (17) of $\widehat{\text{EEC}}$ and $\bar{\chi}^{(100)}$ for a sample size of $N = 100$ are shown in Figures 7 and 8. Taking the diagonal entries gives their variance functions, which are used to construct pointwise confidence bands. The HPE of the EEC has substantially lower variance than the nonparametric sample average estimator, Figures 7 and 8 (right panels). Figures 9 and 10 show simulation results for the pointwise coverage of the true EEC when constructing pointwise 95% confidence bands via (19) and (20). In the top row, the CIs use the "true" variance of the EC curves, estimated by Monte Carlo simulation for a large sample size of 10,000, while in the bottom row, the CIs use the variance estimates corresponding to the given sample size. The coverage function is smoother for the HPE (red) and it guarantees coverage for extreme values of u especially when the variance is estimated from the data. The latter is not the case
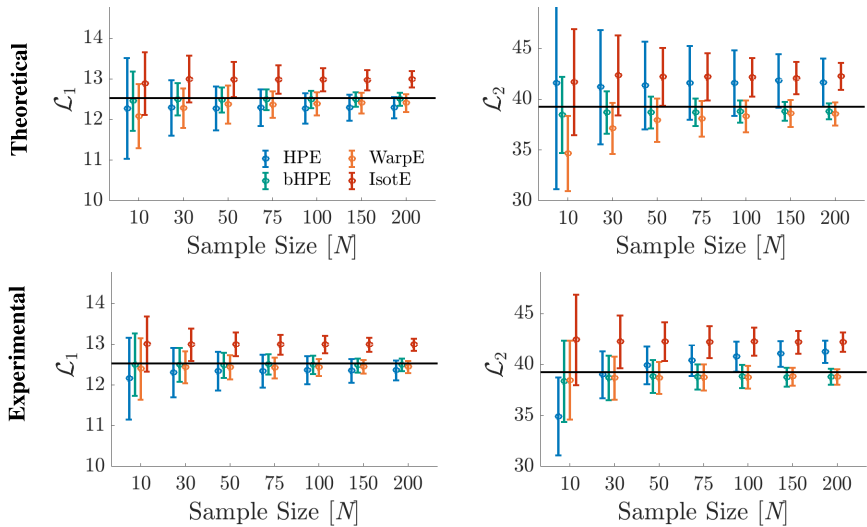
FIG. 6. *Nonstationary non-Gaussian field given by* (31) *for* $L = 10.5$, $A = B = 2.5$ *and* $a = -b = 0.05$ *and using i.i.d. t_3 distributed random variables for generation of the samples*: *comparison of mean and standard deviation of different LKC estimators. Black lines represent the theoretical LKCs.*
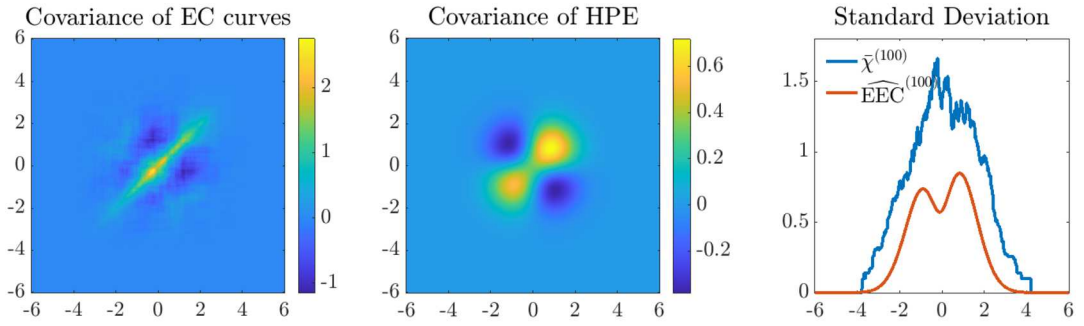
FIG. 7. *Isotropic Gaussian field*: *Covariance functions of the sample average EC curve* (*left*) *and the HPE of the* EEC (*middle*) *from* 100 *samples. Right panel shows their standard deviation functions in red and blue, respectively.*

for the coverage of the CIs from the EC sample average, because large values of u are rarely observed.

In Table 2, we additionally report the coverage of the SCBs discussed in Section 4.2. Here, we again provide Monte Carlo simulations with the asymptotic correct quantile obtained from a χ_2-distribution (compare Proposition 3) assuming the variance to be known and its approximation by the square root of a Hotelling $T_{2,N-1}^2$, if the variance is assumed unknown. In both scenarios, our simulations yield for the isotropic and the nonstationary Gaussian field close to nominal coverage even for sample sizes as small as $N = 10$.

6. Cosmic microwave background radiation. The CMB radiation is the earliest observable radiation and the most important observational probe into the primordial universe. The standard cosmological paradigm, together with inflationary theories, predict the temperature fluctuations in the CMB to be realizations of an isotropic Gaussian random field on the 2-sphere. Comparing the observed CMB map to this theoretical model probes the validity of today's standard cosmological paradigm [1]. There is a long history of anomalous behavior detected in the CMB data with respect to the base model, and their interpretation is a subject of ongoing debate. Some known anomalies that have been confirmed across various data releases from both the WMAP and Planck satellite include the hemispherical power asymmetry [11, 16], the unusual alignment of low multipoles [31], parity violation [11, 23], as well as the slightly unusual behavior of the EEC and the associated Betti numbers [16, 29, 30].

We focus here on the EEC as one commonly used representation of the topological structure of the universe [21]. Our goal is to compare the EC of the observed CMB map to the EEC of simulated maps of the CMB.
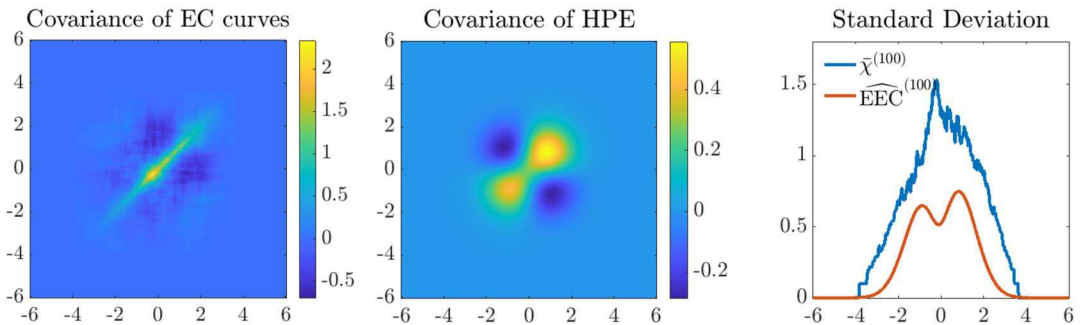

FIG. 8. *Nonstationary Gaussian field*: *Covariance functions of the sample average EC curve* (*left*) *and the HPE of the* EEC (*middle*) *from* 100 *samples. Right panel shows their standard deviation functions in red and blue, respectively.*
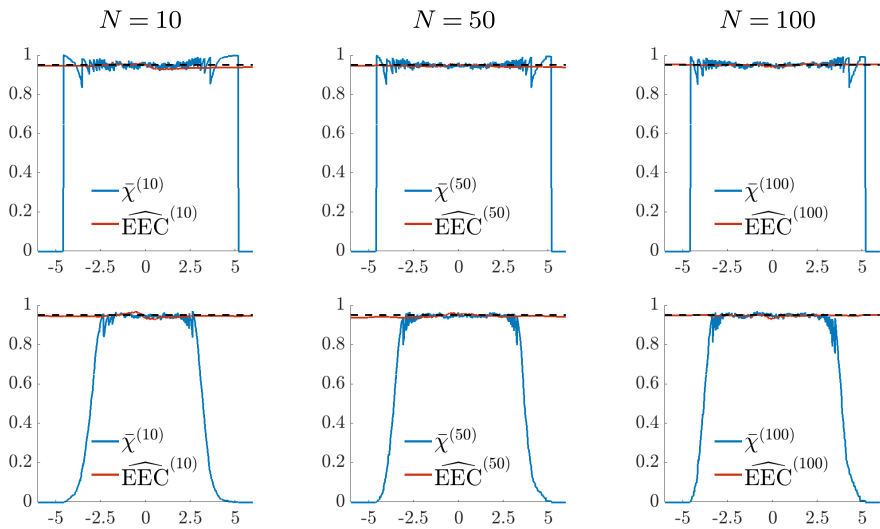
FIG. 9. *Isotropic Gaussian field: pointwise coverage of the EEC under respectively "true" variance of the EC curves (top row) and estimated variance (bottom row) for different sample sizes. The dashed lines represent the target confidence level 95%.*
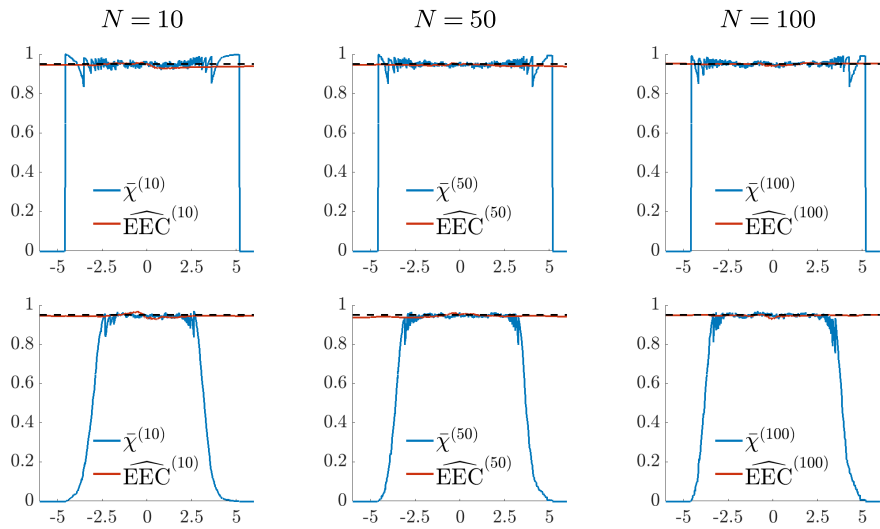

FIG. 10. *Nonstationary Gaussian field: pointwise coverage of the EEC under respectively "true" variance of the EC curves (top row) and estimated variance (bottom row) for different sample sizes. The dashed lines represent the target confidence level 95%.*

TABLE 2
Simulation results of the coverage of the simultaneous 95% confidence bands proposed in (22) using the HPE. The coverage is obtained from 1,000 Monte Carlo simulations

Type	Quantile	Variance	$N = 10$	$N = 50$	$N = 100$
Isotropic Gaussian	$\dfrac{\chi_{2,0.95}}{\sqrt{T_{2,N-1,0.95}^2}}$	true	94.0	94.8	94.7
		estimated	94.9	94.7	93.9
Nonstationary Gaussian	$\dfrac{\chi_{2,0.95}}{\sqrt{T_{2,N-1,0.95}^2}}$	true	95.3	94.6	94.9
		estimated	95.1	93.6	94.4
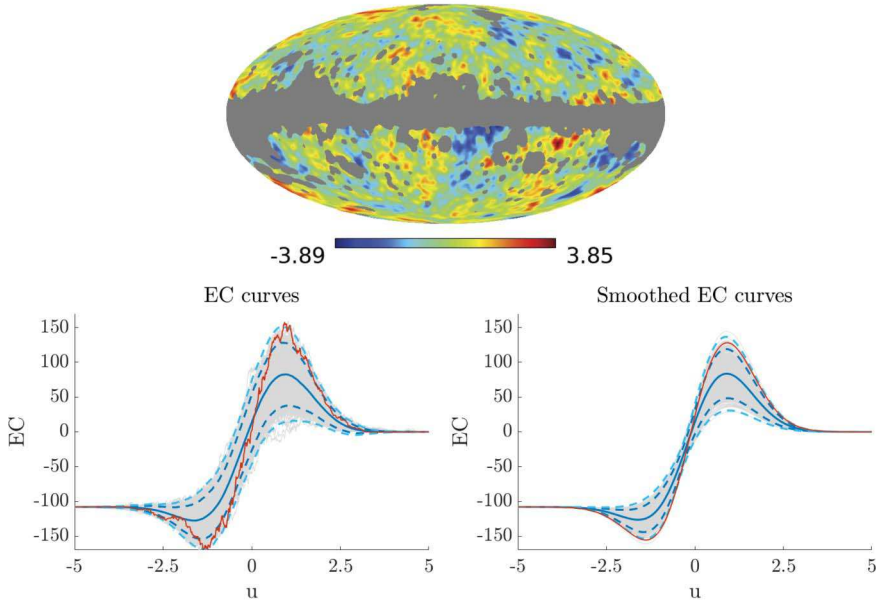
FIG. 11. *CMB example*: (*top*) *cleaned and smoothed observed CMB field.* (*left/right*) *EC curves, raw/ smoothed, simulated CMB fields* (*gray*) *and nonparametric EEC estimate/HPE, with pointwise 2/3-σ-prediction bands* (*blue/light blue*). *The EC curve corresponding to the Planck data is shown in red.*

The observed and simulated maps used here belong to the second public data release (PR2) by the Planck team [2], and are available at https://pla.esac.esa.int/. The simulated maps comprise $N = 1000$ i.i.d. instances of Full Focal Plane 8 (FFP8) simulations. These realistic simulations are realizations of the stationary Gaussian random field having the spatial auto-correlation function and the power spectral density from the observed CMB maps, which are modified according to a model of the measurement process that replicates noise contamination, satellite systematics and the effects of the intervening matter distribution on the CMB light characteristics [6]. As preprocessing, the observed and simulated maps were smoothed with an isotropic Gaussian kernel with a bandwidth of 180 arcmin. The resulting maps are not necessarily samples of a stationary field. Furthermore, the CMB measurement is not reliable in certain parts of the sky, because of contamination by the Milky Way and other bright foreground sources. To exclude these regions from analysis, portions of the sky were masked using the most conservative UT78 mask released by the Planck team [1]. Hence, the simulation and the observed fields are only compared on the subset of the 2-sphere given by the UT78 mask. Figure 11 shows the observed CMB field rendered over a `HealPix` grid with 2048 nodes [19].

The observed and simulated fields were thresholded at a sequence of thresholds ranging from -5 to 5 in steps of 0.01 and the EC of the resulting excursion sets were computed. Figure 11 shows the observed EC curves and their smoothed versions, together with the nonparametric estimate and the HPE of the EEC. We decided to use the HPE instead of the bHPE here, since the simulated data is in fact Gaussian and we can provide estimates of the standard errors (the bHPE is used in the fMRI data analysis) more easily. The estimated LKCs from the FFP8 simulations were $\hat{\mathcal{L}}_1 = 426.8 \pm 54.2$ and $\hat{\mathcal{L}}_2 = 1528.9 \pm 346.4$, yielding respective standard errors of 1.7 and 11.0 for the mean LKCs. In contrast, the estimated LKCs from the actual observed field were $\hat{\mathcal{L}}_1^o = 480.3$ and $\hat{\mathcal{L}}_2^o = 2545.0$.

These results have two uses in astronomy. First, the EEC could be used to detect celestial objects against the CMB background [10]. In this case, we obtain $u_{\text{FWER}} = 4.279 \pm 0.002$ and $u_{\text{CER}} = 3.456 \pm 0.002$. Second, in Figure 11, the observed CMB EC curve (red) is at

the edge of the distribution of simulated curves. In fact, the observed $\hat{\mathcal{L}}_2^o$ is 2.93 standard deviations away from $\hat{\mathcal{L}}_2$. This may be evidence that the observed CMB field does not match the theoretical model that generated the simulations. However, it is unclear whether the mismatch is due to the parts of the model related to the physics of the early universe or the parts related to the measurement process. A more detailed investigation, as well as an analysis of the latest data releases by the Planck team, which will be undertaken in future works, will serve to substantiate the veracity of our claims.

7. Discussion.   This article studied estimation of LKC and thereby EECs for Gaussian and non-Gaussian fields. In particular, it introduced an alternative to the WarpE to estimate the LKCs of a limiting process from observed nonstationary random fields. Our simulations showed that the bHPE has a similar variance as the WarpE, which computes a discrete version of $\mathcal{L}(\hat{\mathfrak{r}}^{(N)})$. Hence, for a fixed sample, although being completely differently computed, the WarpE and the bHPE are numerically similar. This distinguishes the bHPE from the HPE, since the source of variability in the latter is the variability in the observed EC curves, while in the former variability is due to the variability of the covariance estimate $\hat{\mathfrak{r}}^{(N)}$. Understanding why the former is lower requires a deeper study of the probabilistic theory of excursion sets.

The main advantage of the HPE/bHPE compared to the WarpE is that it is conceptually and computationally simpler. It allows the fields to be defined over nontrivial domains, like subdomains of the sphere, the highly curved cortical surface of the brain or any D-dimensional manifold and the estimation procedure only depends on an algorithm to compute the EC of excursion sets, for which general and efficient algorithms exist, for example, [20]. Therefore, it is a good alternative in situations like the CMB observations in astronomy, where the EC curves are efficiently computed, while a triangulation and computation of the involved geometric quantities in the embedding space, required for the WarpE, are usually not accessible. A further advantage of the HPE/bHPE is that we were able to study theoretical properties such as unbiasedness, finite variance and consistency, and derive CLTs and confidence bands for the EEC. Similar theoretical analyses were only partially feasible for the WarpE; see [35]. Last but not least, we believe that all presented results generalize to S being a compact, regular, stratified manifold. The latter is immediately clear for Theorems 1 and 2 as the normal Morse indices are bounded from above and below by $\pm C$ for some $C > 0$. The latter follows from the definition of the normal Morse index and the fact that any regular, stratified manifold is a union of finitely many (path-connected) manifolds without boundary. The only technical difficulty in generalizing Theorem 3 lies in proving a.s. convergence (or convergence in probability) of the normal Morse index which under Assumption (**R**) should hold.

SUPPLEMENTARY MATERIAL

Supplement to "Estimation of Expected Euler Characteristic Curves of Nonstationary Smooth Random Fields" (DOI: 10.1214/23-AOS2337SUPP; .pdf). Appendix A: Additional material on theory, among others, describing the connection of the HPE to LKC regression, efficient computation of EC curves, sufficient conditions for (**G4**) and a general example such that the GMF satisfies the GKF. Appendix B: Additional simulations showing the dependence on resolution, the connectivity criterion, the choice of the bootstrap multipliers and the number of bootstrap replicates. It also contains another nonstationary (non-Gaussian) LKC estimation example. Appendix C: LKC estimation for general linear models and a data analysis application to fMRI data. Appendix D: Proofs of all theorems from the main manuscript.

REFERENCES

[1] ADE, P. A., AGHANIM, N., ARMITAGE-CAPLAN, C., ARNAUD, M., ASHDOWN, M., ATRIO-BARANDELA, F., AUMONT, J., BACCIGALUPI, C., BANDAY, A. J. et al. (2014). Planck 2013 results. XXIII. Isotropy and statistics of the CMB. *Astron. Astrophys.* **571** A23.

[2] ADE, P. A., AGHANIM, N., ARNAUD, M., ASHDOWN, M., AUMONT, J., BACCIGALUPI, C., BANDAY, A., BARREIRO, R., BARTLETT, J. et al. (2016). Planck 2015 results-XII. Full focal plane simulations. *Astron. Astrophys.* **594** A12.

[3] ADLER, R. J. (1977). A spectral moment estimation problem in two dimensions. *Biometrika* **64** 367–373. MR0466102 https://doi.org/10.1093/biomet/64.2.367

[4] ADLER, R. J., BARTZ, K., KOU, S. C. and MONOD, A. (2017). Estimating thresholding levels for random fields via Euler characteristics. ArXiv preprint. Available at arXiv:1704.08562.

[5] ADLER, R. J. and TAYLOR, J. E. (2007). *Random Fields and Geometry. Springer Monographs in Mathematics*. Springer, New York. MR2319516

[6] BARTLETT, J., BUCHER, M., CARDOSO, J., CASTEX, G., DELABROUILLE, J., GANGA, K., GIRAUD-HÉRAUD, Y., LE JEUNE, M., PATANCHON, G. et al. (2016). Planck 2015 results: IX. Diffuse component separation: CMB maps. *Astron. Astrophys.* **594** A9–A9.

[7] BIERMÉ, H., DI BERNARDINO, E., DUVAL, C. and ESTRADE, A. (2019). Lipschitz–Killing curvatures of excursion sets for two-dimensional random fields. *Electron. J. Stat.* **13** 536–581. MR3911693 https://doi.org/10.1214/19-EJS1530

[8] BULLMORE, E. T., SUCKLING, J., OVERMEYER, S., RABE-HESKETH, S., TAYLOR, E. and BRAMMER, M. J. (1999). Global, voxel, and cluster tests, by theory and permutation, for a difference between two groups of structural MR images of the brain. *IEEE Trans. Med. Imag.* **18** 32–42. https://doi.org/10.1109/42.750253

[9] CABAÑA, E. M. (1985). Estimation of the spectral moment by means of the extrema. *Trabajos de Estadística e Investigación Operativa* **36** 71–80.

[10] CHENG, D., CAMMAROTA, V., FANTAYE, Y., MARINUCCI, D. and SCHWARTZMAN, A. (2020). Multiple testing of local maxima for detection of peaks on the (celestial) sphere. *Bernoulli* **26** 31–60. MR4036027 https://doi.org/10.3150/18-BEJ1068

[11] COLLABORATION, P., ADE, P. A. R., AGHANIM, N., ARMITAGE-CAPLAN, C., ARNAUD, M., ASHDOWN, M., ATRIO-BARANDELA, F., AUMONT, J., BACCIGALUPI, C. et al. (2014). Planck 2013 results. XXIII. Isotropy and statistics of the CMB. *Astron. Astrophys.* **571** A23.

[12] DAVENPORT, S. and TELSCHOW, F. J. (2022). On the finiteness of second moments of the number of critical points of Gaussian random fields. ArXiv preprint. Available at arXiv:2201.01591.

[13] DEGRAS, D. A. (2011). Simultaneous confidence bands for nonparametric regression with functional data. *Statist. Sinica* **21** 1735–1765. MR2895997 https://doi.org/10.5705/ss.2009.207

[14] DI BERNARDINO, E., ESTRADE, A. and LEÓN, J. R. (2017). A test of Gaussianity based on the Euler characteristic of excursion sets. *Electron. J. Stat.* **11** 843–890. MR3629017 https://doi.org/10.1214/17-EJS1248

[15] EKLUND, A., NICHOLS, T. E. and KNUTSSON, H. (2016). Cluster failure: Why fMRI inferences for spatial extent have inflated false-positive rates. *Proc. Natl. Acad. Sci. USA* **113** 7900–7905.

[16] ERIKSEN, H. K., HANSEN, F. K., BANDAY, A. J., GÓRSKI, K. M. and LILJE, P. B. (2004). Asymmetries in the Cosmic Microwave Background Anisotropy Field. *Astrophys. J.* **605** 14–20.

[17] GASS, L. and STECCONI, M. (2023). The number of critical points of a Gaussian field: Finiteness of moments. ArXiv preprint. Available at arXiv:2305.17586.

[18] GORESKY, M. and MACPHERSON, R. (1988). *Stratified Morse Theory. Ergebnisse der Mathematik und Ihrer Grenzgebiete* (3) [*Results in Mathematics and Related Areas* (3)] **14**. Springer, Berlin. MR0932724 https://doi.org/10.1007/978-3-642-71714-7

[19] GORSKI, K. M., HIVON, E., BANDAY, A. J., WANDELT, B. D., HANSEN, F. K., REINECKE, M. and BARTELMANN, M. (2005). HEALPix: A framework for high-resolution discretization and fast analysis of data distributed on the sphere. *Astrophys. J.* **622** 759.

[20] HEISS, T. and WAGNER, H. (2017). Streaming algorithm for Euler characteristic curves of multidimensional images. In *Computer Analysis of Images and Patterns. Part I. Lecture Notes in Computer Science* **10424** 397–409. Springer, Cham. MR3695725 https://doi.org/10.1007/978-3-319-64689-3

[21] HIKAGE, C., SUTO, Y., KAYO, I., TARUYA, A., MATSUBARA, T., VOGELEY, M. S., HOYLE, F., GOTT III, J. R., BRINKMANN, J. et al. (2002). Three-dimensional genus statistics of galaxies in the SDSS early data release. *Publ. Astron. Soc. Jpn.* **54** 707–717.

[22] KIEBEL, S. J., POLINE, J. B., FRISTON, K. J., HOLMES, A. P. and WORSLEY, K. J. (1999). Robust smoothness estimation in statistical parametric maps using standardized residuals from the general linear model. *NeuroImage* **10** 756–766. https://doi.org/10.1006/nimg.1999.0508

[23] LAND, K. and MAGUEIJO, J. (2005). Is the universe odd? *Phys. Rev. D* **72** 101302. MR2188178 https://doi.org/10.1103/PhysRevD.72.101302

[24] LIEBL, D. and REIMHERR, M. (2023). Fast and fair simultaneous confidence bands for functional parameters. *J. R. Stat. Soc. Ser. B. Stat. Methodol.* **85** 842–868. https://doi.org/10.1093/jrsssb/qkad026

[25] MILNOR, J. (1963). *Morse Theory. Annals of Mathematics Studies, No.* 51. Princeton Univ. Press, Princeton, NJ. MR0163331

[26] MORAN, J. M., JOLLY, E. and MITCHELL, J. P. (2012). Social-cognitive deficits in normal aging. *J. Neurosci.* **32** 5553–5561.

[27] NICHOLS, T. E. (2012). Multiple testing corrections, nonparametric methods, and random field theory. *NeuroImage* **62** 811–815. https://doi.org/10.1016/j.neuroimage.2012.04.014

[28] PITERBARG, V. (1996). Rice's method for large excursions of Gaussian random fields. Technical Report 478, Center for Stochastic Processes, Univ. North Carolina.

[29] PRANAV, P. (2022). Anomalies in the topology of the temperature fluctuations in the cosmic microwave background: An analysis of the NPIPE and FFP10 data releases. *Astron. Astrophys.* **659** A115.

[30] PRANAV, P., ADLER, R. J., BUCHERT, T., EDELSBRUNNER, H., JONES, B. J., SCHWARTZMAN, A., WAGNER, H. and VAN DE WEYGAERT, R. (2019). Unexpected topology of the temperature fluctuations in the cosmic microwave background. *Astron. Astrophys.* **627** A163.

[31] SCHWARZ, D. J., COPI, C. J., HUTERER, D. and STARKMAN, G. D. (2016). CMB anomalies after Planck. *Classical Quantum Gravity* **33** 184001.

[32] SOMMERFELD, M., SAIN, S. and SCHWARTZMAN, A. (2018). Confidence regions for spatial excursion sets from repeated random field observations, with an application to climate. *J. Amer. Statist. Assoc.* **113** 1327–1340. MR3862360 https://doi.org/10.1080/01621459.2017.1341838

[33] TAYLOR, J., TAKEMURA, A. and ADLER, R. J. (2005). Validity of the expected Euler characteristic heuristic. *Ann. Probab.* **33** 1362–1396. MR2150192 https://doi.org/10.1214/009117905000000099

[34] TAYLOR, J. E. (2006). A Gaussian kinematic formula. *Ann. Probab.* **34** 122–158. MR2206344 https://doi.org/10.1214/009117905000000594

[35] TAYLOR, J. E. and WORSLEY, K. J. (2007). Detecting sparse signals in random fields, with an application to brain mapping. *J. Amer. Statist. Assoc.* **102** 913–928. MR2354405 https://doi.org/10.1198/016214507000000815

[36] TELSCHOW, F. J, CHENG, D., PRANAV, P. and SCHWARTZMAN, A. (2023). Supplement to "Estimation of Expected Euler Characteristic Curves of Nonstationary Smooth Random Fields." https://doi.org/10.1214/23-AOS2337SUPP

[37] TELSCHOW, F. J. E., DAVENPORT, S. and SCHWARTZMAN, A. (2022). Functional delta residuals and applications to simultaneous confidence bands of moment based statistics. *J. Multivariate Anal.* **192** Paper No. 105085. MR4463046 https://doi.org/10.1016/j.jmva.2022.105085

[38] TELSCHOW, F. J. E., PIERRYNOWSKI, M. R. and HUCKEMANN, S. F. (2023). Confidence tubes for curves on SO(3) and identification of subject-specific gait change after kneeling. *J. R. Stat. Soc. Ser. C. Appl. Stat.* qlad060.

[39] TELSCHOW, F. J. E. and SCHWARTZMAN, A. (2022). Simultaneous confidence bands for functional data using the Gaussian kinematic formula. *J. Statist. Plann. Inference* **216** 70–94. MR4273839 https://doi.org/10.1016/j.jspi.2021.05.008

[40] WORSLEY, K. J., EVANS, A. C., MARRETT, S. and NEELIN, P. (1992). A three-dimensional statistical analysis for CBF activation studies in human brain. *J. Cereb. Blood Flow Metab.* **12** 900–918.

[41] WORSLEY, K. J., MARRETT, S., NEELIN, P., VANDAL, A. C., FRISTON, K. J. and EVANS, A. C. (1996). A unified statistical approach for determining significant signals in images of cerebral activation. *Hum. Brain Mapp.* **4** 58–73.

[42] WORSLEY, K. J., TAYLOR, J. E., TOMAIUOLO, F. and LERCH, J. (2004). Unified univariate and multivariate random field theory. *NeuroImage* **23** S189–S195.